Research Square

Preprints are preliminary reports that have not undergone peer review.
They should not be considered conclusive, used to inform clinical practice,
or referenced by the media as validated information.

Bioactive 3D-Printed Composite Scaffolds Based on Hydrogels Containing Grape Peel Extract-Loaded Silica Nanoparticles for Drug Delivery and Tissue Engineering

Andreea Trifan
Universitatea Națională de Știință și Tehnologie Politehnica București
Andra-Maria Pavel
Universitatea Națională de Știință și Tehnologie Politehnica București
Daniela Berger
Universitatea Națională de Știință și Tehnologie Politehnica București
Roxana-Cristina Popescu
Horia Hulubei National Institute for R and D in Physics and Nuclear Engineering
Doru-Daniel Cristea
Carol Davila University of Medicine and Pharmacy
Ciprian-Ștefan Mateescu
Carol Davila University of Medicine and Pharmacy
Eduard Liciu
eduard.liciu@umfcd.ro

Carol Davila University of Medicine and Pharmacy
Cristina Busuioc
Universitatea Națională de Știință și Tehnologie Politehnica București

Research Article

Keywords: 3D-printed scaffolds, silica nanoparticles, composite hydrogels, grape peel extract, biopolymers, tissue engineering

Posted Date: September 2nd, 2026

DOI: https://doi.org/10.21203/rs.3.rs-10508372/v1

License: This work is licensed under a Creative Commons Attribution 4.0 International License.
Read Full License

Additional Declarations: No competing interests reported.

Bioactive 3D-Printed Composite Scaffolds Based on Hydrogels Containing Grape Peel Extract-Loaded Silica Nanoparticles for Drug Delivery and Tissue Engineering

Andreea Trifan[1,2,3] · Andra-Maria Pavel[4] · Daniela Berger[1] · Roxana-Cristina Popescu[4,5] · Doru-Daniel Cristea[2,6] · Ciprian-Ștefan Mateescu[2,6] · Cristina Busuioc[1,3*] · Eduard Liciu[2,*]

Abstract

This study developed composite scaffolds based on alginate–gelatine–xanthan gum hydrogels incorporating grape (*Vitis vinifera* L.) peel extract-loaded mesoporous silicon dioxide (SiO_2) nanoparticles and assessed their initial cytocompatibility toward mouse preosteoblastic MC3T3-E1 cells. Mesoporous SiO_2 nanoparticles were synthesized by a cetyltrimethylammonium bromide-templated sol–gel route using tetraethyl orthosilicate (TEOS) : cetyltrimethylammonium bromide (CTAB) molar ratios of 2:1 and 4:1, calcined at 550 degrees Celsius, and loaded with Soxhlet-derived grape peel extract, then dispersed in hydrogels and printed into cylindrical scaffolds. Both SiO_2 formulations yielded predominantly amorphous mesoporous carriers with type IV nitrogen adsorption–desorption isotherms and pore sizes of 3.5 to 4 nm, efficiently loaded with grape peel polyphenols. SiO_2-reinforced scaffolds showed reduced swelling and slower mass loss over 30 days in phosphate-buffered saline, together with time-dependent release of ultraviolet-active species. Lactate dehydrogenase release remained below the cytotoxicity threshold for MC3T3-E1 cells, and scanning electron microscopy confirmed preosteoblastic cell attachment within the interconnected macroporous network. These findings support the potential of grape peel extract-loaded mesoporous silicon dioxide–reinforced hydrogels as bioactive 3D-printed scaffolds for tissue engineering.

Keywords 3D-printed scaffolds · silica nanoparticles · composite hydrogels · grape peel extract · biopolymers · tissue engineering

1. Introduction

The global wine and food industry generates vast quantities of grape pomace [1] — the solid residue comprising skins, seeds, and pulp [2] remaining after pressing — representing a major source of agro-industrial waste [3] that poses significant environmental and waste-management challenges [4]. This by-product of *Vitis vinifera* L. processing [5] has increasingly attracted research attention as a valuable feedstock for the recovery of bioactive polyphenolic compounds [6], most notably *trans*-resveratrol (*trans*-3,5,4'-trihydroxystilbene) [7], a phytoalexin naturally synthesized by the grapevine in response to biotic and abiotic stressors [8] including fungal infection [2], ultraviolet (UV) irradiation [9], and mechanical injury [6].

Of particular relevance to tissue repair and regenerative medicine is the dual capacity of resveratrol to simultaneously inhibit angiogenesis in tumour contexts [8] — through downregulation of vascular endothelial growth factor (VEGF) [10], hypoxia-inducible factor 1-alpha (HIF-1α), and matrix metallopeptidase 2 (MMP-2) activity [11] and to promote physiological angiogenesis [12] in wound healing contexts through VEGF upregulation [10] and stimulation of endothelial progenitor cell function [13]. This dual angiogenic modulatory role positions resveratrol as a uniquely attractive bioactive agent [14] for scaffolds targeting vascularized tissue regeneration [15], where adequate neovascularization is a recognized rate-limiting step for defect healing.

Soxhlet extraction [16] from dried and ground grape peel represents a well-established and reproducible approach for isolating polyphenol-rich fractions [17], offering a controlled extraction environment that

Correspondence: Cristina Busuioc: cristina.busuioc@upb.ro
Eduard Liciu, eduard.liciu@umfcd.ro

1 Faculty of Chemical Engineering and Biotechnologies, National University of Science and Technology Politehnica Bucharest, 011061, Romania
2 3D Printing Laboratory, Center of Innovation and e-Health, Carol Davila University of Medicine and Pharmacy, Bucharest, 020021, Romania
3 National Center of Micro and Nanomaterials, National University of Science and Technology Politehnica Bucharest, 060042 Bucharest, Romania
4 Faculty of Medical Engineering, National University of Science and Technology Politehnica Bucharest, 011061, Bucharest, Romania
5 "Horia Hulubei" National Institute of Physics and Nuclear Engineering, 077125, Magurele, Romania
6 REOROM Laboratory, Hydraulics Department, National University of Science and Technology Politehnica Bucharest, 060042, Bucharest, Romania

concentrates stilbenes and related phenolics from the solid matrix into an ethanolic or methanolic solvent phase. Beyond its role as a phytoalexin, resveratrol exhibits a broad and well-documented spectrum of pharmacological activities [8], encompassing antioxidant [6], anti-inflammatory [18], anticancer [19], cardioprotective [8], and neuroprotective effects [18], all of which render it a compelling bioactive compound [12] for incorporation into advanced drug delivery platforms [11]. However, the clinical and biomedical translation of resveratrol remains substantially impeded by its inherent physicochemical limitations [5]: low aqueous solubility (~30 μg/mL)[4], rapid photoisomerization from the biologically active *trans*- to the less active *cis*-form upon UV exposure [20], chemical instability at alkaline pH, and extensive first-pass glucuronidation [21] and sulfation yielding a plasma half-life of only 8–14 min following systemic administration.

To overcome these challenges, integration of resveratrol within silica (SiO_2) [22] particles has emerged as a promising strategy. The inorganic, sol-gel derived SiO_2 network provides a porous framework that physically protects the molecule from photodegradation [23], and modulates its release through diffusion-controlled kinetics [24] governed by hydrogen bonding interactions [25] between the drug's hydroxyl groups and the silanol surface groups [26] of the SiO_2 matrix. When incorporated into a 3D hydrogel scaffold [27], the SiO_2 phase further confers mechanical reinforcement [28] to an otherwise mechanically compliant hydrogel matrix, while the hydrogel component provides the high water content, viscoelastic behaviour [29], and cell-compatible microenvironment required for tissue engineering applications [30].

Extrusion-based 3D bioprinting [31] offers a clinically and industrially scalable fabrication route for such composite scaffolds [32], enabling precise spatial control of pore architecture [18], filament diameter [33], and scaffold geometry according to patient-specific anatomical data [28], while accommodating the rheological requirements [35, 36] of viscous hydrogel bioinks without the photocytotoxic risk associated with photopolymerization-based methods [36].

The present study therefore aims to valorise *Vitis vinifera* L. peel through Soxhlet extraction to obtain a resveratrol-enriched polyphenolic extract; incorporate this extract into a SiO_2 composite hydrogel formulation suitable for extrusion-based 3D printing; characterize the physicochemical, structural, mechanical, and drug-release properties of the resulting scaffolds; and evaluate the *in vitro* bioactivity, testing the hypothesis that the sustained local release of resveratrol from the 3D-printed SiO_2 composite scaffold will support cell response, thereby providing a multifunctional biomaterial platform combining waste valorisation, controlled drug delivery, and regenerative bioactivity.

2. Materials and methods

2.1 Materials

Tetraethyl orthosilicate (TEOS, $Si(OC_2H_5)_4$, ≥98 %, Sigma-Aldrich, St. Louis, MO, USA) was used as the SiO_2 alkoxide precursor. Cetyltrimethylammonium bromide (CTAB, $C_{16}H_{33}N(CH_3)_3Br$, ≥99 %, Sigma-Aldrich, St. Louis, MO, USA) served as the structure-directing surfactant template. Ammonium hydroxide solution (25% NH_3(aq), Chimreactiv S.R.L., Bucharest, Romania) was used as the basic catalyst for hydrolysis and condensation. Sodium alginate, xanthan gum, and gelatine from porcine skin served as the biopolymer components of the hydrogel matrix; sodium alginate and xanthan gum were purchased from Sigma-Aldrich (St. Louis, MO, USA), while gelatine was acquired from Merck (Darmstadt, Germany). Ethanol (C_2H_5OH, 98%), calcium chloride ($CaCl_2$, ≥93.0%, anhydrous, granular) and glutaraldehyde solution (50% in water, 5.6 M), used as solvent and crosslinking agents, respectively, were purchased from Sigma-Aldrich (St. Louis, MO, USA). Phosphate-buffered saline (PBS 10×, Remed Lab, Bucharest, Romania) was diluted with distilled water to obtain PBS 1× (pH 7.4) and used as the aqueous medium for hydrogel preparation. Dark table grapes of the Hamburg variety (*Vitis vinifera* L.) were purchased from a local market and used as the plant source for polyphenol extraction. Regarding cell studies, Minimum Essential Medium Alpha (*α*-MEM, Gibco), foetal bovine serum (FBS), *L*-glutamine, penicillin–streptomycin, dimethyl sulfoxide (DMSO), hexamethyldisilazane (HMDS), and the Lactate Dehydrogenase (LDH) Cytotoxicity Assay kit were purchased from Thermo Fisher Scientific (Waltham, MA, USA).

2.2 Synthesis of mesoporous SiO_2 nanoparticles

SiO_2 nanoparticles were synthesized by a CTAB–assisted sol–gel method in two formulations, using TEOS:CTAB molar ratios of 2:1 and 4:1, in order to obtain carriers with distinct porous architectures, as shown in Fig. 1. For each formulation, 100 mL of ethanol and 240 mL of distilled water were combined and homogenised under magnetic stirring for 30 min. CTAB was then added and dissolved completely to form a clear micellar solution. The reaction medium was subsequently alkalinised by the gradual addition of 24 mL of ammonium hydroxide solution to reach a basic pH of 10–11, creating conditions favourable for TEOS hydrolysis and condensation. TEOS (7.4 mL for both formulations)

was added dropwise under continuous magnetic stirring at room temperature, followed by gel formation. The resulting material was collected by filtration, washed repeatedly with distilled water and ethanol to remove residual ammonia, unreacted precursor, and organic impurities, and dried in a ventilated oven at 100 °C until constant mass. The dried powder was subsequently calcined at 550 °C in air using a slow heating ramp to remove the CTAB template completely and generate the open mesoporous structure characteristic of MCM-41-type SiO_2.

2.3 Preparation of grape extract by Soxhlet extraction

Approximately 1000 g of whole grapes were thoroughly washed with tap water followed by distilled water, and then air-dried. The fruits were placed in a ventilated oven and dried at 48 °C for 5 days. Dried grapes were manually separated into skins and seeds, where the peels were then ground to a fine powder using a laboratory mill and passed through a mesh sieve. 10 g of powdered material were transferred into a cellulose extraction thimble and subjected to Soxhlet extraction with a hydroalcoholic solvent consisting of 160 mL ethanol (80% v/v) and 40 mL distilled water, for 6–8 h, to ensure continuous siphoning.

2.4 Loading of grape extract into SiO_2 nanoparticles

SiO_2 powder was dried prior to loading, at 60 °C overnight to remove adsorbed moisture and ensure maximum pore accessibility. An accurately weighed amount of pre-dried SiO_2 was dispersed into the grape extract solution at a solid-to-solution ratio of 1:10 (w/v; 1 g SiO_2 per 10 mL extract solution). Suspensions were prepared in glass containers wrapped in aluminium foil to minimise light exposure, and maintained at room temperature under gentle magnetic stirring for 24 h to allow diffusion and adsorption of polyphenolic constituents, into the mesopores. Subsequently, the extract-loaded SiO_2 was recovered by filtration, briefly rinsed once with ethanol to remove loosely surface-adsorbed extract, and dried at 40 °C for 24 h in a ventilated oven. During drying, containers were kept sealed and fully wrapped in aluminium foil to prevent light-induced degradation. The resulting grape peel extract-loaded SiO_2 powders were gently ground to break up soft agglomerates and transferred to sealed foil-wrapped containers until further use.

2.5 Preparation of composite hydrogel formulations

Polymers and SiO_2 powders were weighed separately according to Table 1. For composite formulations, grape peel extract loaded-SiO_2 was first dispersed in freshly prepared PBS 1× under magnetic stirring at room temperature for 15 min. Xanthan gum was then added gradually under continuous stirring, and the system was mixed until complete solubilization. The temperature was raised to 36 °C, and gelatine was added in small portions with stirring until fully dissolved and sodium alginate was finally incorporated gradually under magnetic stirring, yielding a uniform, opalescent composition, as shown in Fig. 1. The resulting composite inks were stored overnight at 4 °C to promote polymer network consolidation prior to printing. During this cold–gelation step, gelatine and alginate form interpenetrating polymer networks, which improves the structural integrity and printability of the inks.

Table 1. Composition of the printable inks.

Sample name	Sodium alginate (wt%)	Gelatine (wt%)	Xanthan gum (wt%)	SiO_2 4:1 (wt%)	SiO_2 2:1 (wt%)
P1	4	6	2	0	0
P2	4	6	2	2.0	0
P3	4	6	2	0	2.0
P4	4	8	2	0	0
P5	4	8	2	0.5	0
P6	4	8	2	0	0.5

2.6 3D printing and post-print stabilization of scaffolds

Hydrogel and composite inks (P1–P6) were loaded into 3 mL printing cartridges and extruded using a pneumatic extrusion-based 3D bioprinter (Bio X, Cellink, Gothenburg, Sweden) equipped with 25G polyethylene nozzles (inner diameter 250 μm). G-code files were generated using DNA Studio v4.3.5 (Cellink, Gothenburg, Sweden). Two scaffold architectures were printed for each formulation: square-grid constructs (10×10×3 mm^3) with a rectilinear infill pattern, used for the evaluation of filament diameter, strand uniformity, and pore geometry; and cylindrical constructs (diameter 10 mm × height 3 mm, 12 layers, 30 % infill density, gyroid morphology), used for functional characterisation including swelling, degradation, and biological assays.

Air pressures and print speeds were adjusted per formulation, as summarised in Table 2. Immediately after printing, constructs were crosslinked for 5 min in a solution of 1.5 wt% $CaCl_2$ and 0.5 wt% glutaraldehyde to promote ionic crosslinking of alginate and chemical crosslinking of gelatine, then washed with demineralised water and stored at 24 °C under controlled humidity.

Table 2. Extrusion 3D printing parameters used for the scaffolds P1-P6.

Sample name	Grid printing speed (mm/s)	Grid printing pressure (kPa)	Scaffold printing speed (mm/s)	Scaffold printing pressure (kPa)
P1	12	147	11	247
P2	8	277	8	298
P3	9	249	9	360
P4	11	180	11	265
P5	11	240	8	270
P6	10	260	7	281

2.7 Physicochemical characterization

2.7.1 Thermal analysis

Thermal stability of the uncalcined powders was evaluated by simultaneous thermogravimetric analysis (TGA), differential thermogravimetry (DTG), and differential scanning calorimetry (DSC) using a STA 449 F3 Jupiter instrument (NETZSCH, Selb, Germany), from room temperature to 900 °C at a heating rate of 10 °C/min in air. This combined approach enabled separation of mass loss events and guided the choice of the calcination regime.

2.7.2 Fourier transform infrared spectroscopy

Fourier transform infrared spectroscopy (FTIR) was performed in attenuated total reflectance (ATR) mode using a Nicolet iS50 spectrometer (Thermo Scientific, Waltham, MA, USA) over the range 4000–400 cm^{-1} at 4 cm^{-1} resolution with 32 scans per sample, and was used to identify characteristic functional groups and intermolecular interactions among SiO_2 powders and 3D-printed scaffolds containing sodium alginate, gelatin, xanthan gum.

2.7.3 X-ray diffraction

The crystalline or amorphous nature of the SiO_2 powders after calcination was investigated by X-ray diffraction (XRD) using a Shimadzu XRD-6000 diffractometer (Shimadzu Corporation, Kyoto, Japan) with Cu Kα radiation (λ = 0.154 nm) over a 2θ range of 10–70 ° with a step size of 0.02 °.

2.7.4 Energy-dispersive X-ray spectroscopy and scanning electron microscopy

The elemental composition was assessed by energy-dispersive X-ray spectroscopy (EDS) and the morphology of both mesoporous SiO_2 particles and 3D-printed scaffolds was examined by scanning electron microscopy (SEM), using a FEI Quanta Inspect F50 scanning electron microscope (FEI Company, Hillsboro, OR, USA).

2.7.5 Nitrogen adsorption/desorption isotherms

Specific surface area using Brunauer–Emmett–Teller (BET) method, total pore volume recorded at relative pressure of 0.99, and pore size distribution curves of the calcined SiO_2 powders were determined by nitrogen adsorption–desorption isotherms recorded at 77 K (Micromeritics TriStar II Plus surface area and porosity analyzer). The samples were degassed at 110 °C for 17 h under vacuum prior to measurement. The pore size distribution curves were derived from the desorption branch using the Barrett–Joyner–Halenda (BJH) method.

2.7.6 UV–Vis spectroscopy

UV-Vis absorption spectra were recorded on a double-beam spectrophotometer in the range 200–450 nm at 1 nm step size using quartz cuvettes with a 1 cm path length, using the Soxhlet-derived grape peel extract. For the assessment of extract uptake by the SiO_2 carriers, the spectra were recorded on the residual supernatant (filtrate) collected after the 24 h adsorption period and subsequent recovery of the loaded SiO_2 powder by filtration. Regarding the release-profile of the composite scaffolds, measurements of P2 and P3 were collected at multiple time points (0, 30, 60, 90, 120, 150, and 180 min).

2.7.7 Rheological characterization

Rheological characterization of the viscoelastic [37] printable inks was performed using a systematic set of tests designed to capture the mechanical behaviour under oscillatory and steady-shear conditions. Before measurement, the material was equilibrated at the testing temperature for 2 min. A thin layer of vegetable oil was applied to the sample surface to prevent hydrogel drying during the experiment. Rheological analyses were carried out using an Anton Paar rheometer (Anton Paar GmbH, Graz, Austria) fitted with a 25 mm parallel-plate geometry, where the sample was loaded onto the lower plate with a gap of 0.5 mm. All measurements were carried out at $25 \pm 0.1\,℃$, maintained using a temperature-controlled Peltier system.

Amplitude sweep tests were first performed at a constant angular frequency of $\omega = 1\ s^{-1}$ to determine the linear viscoelastic region (LVR) of each sample. The LVR corresponds to the strain range over which the material structure remains intact, and the viscoelastic moduli are independent of strain amplitude. Frequency sweep measurements were then conducted at a fixed strain amplitude of $\gamma = 0.0001$, selected to remain within the previously established LVR. Finally, steady shear tests were performed to evaluate the variation in viscosity as a function of shear rate [38].

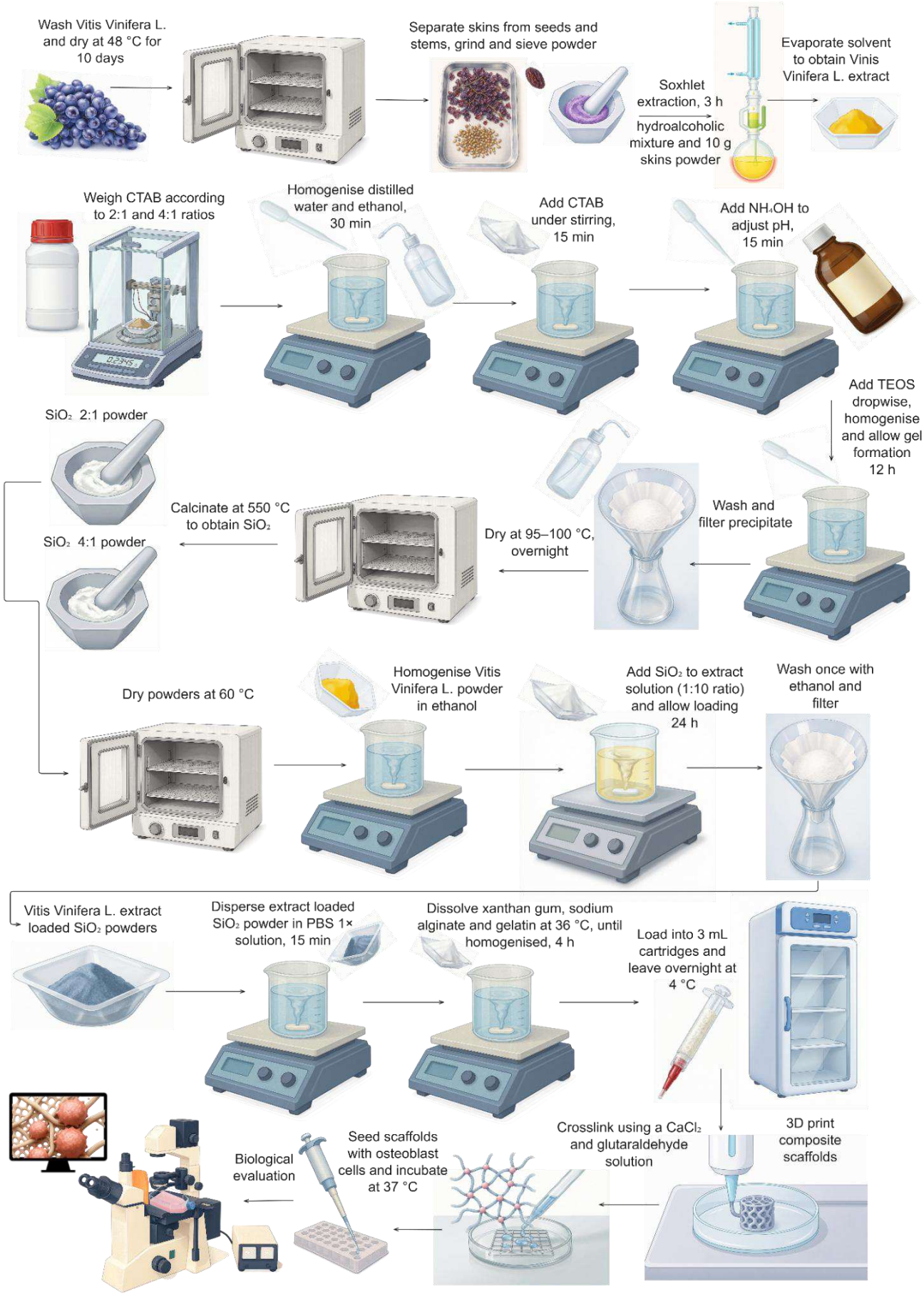


Fig. 1. Schematic workflow for the fabrication of *Vitis vinifera* L. extract-loaded scaffolds. Illustration of grape waste valorisation, sol–gel SiO_2 synthesis and loading, Alg/Gel/XG hydrogel preparation, extrusion-based 3D printing, crosslinking with calcium chloride, and subsequent biological evaluation of the printed scaffolds, made using Illustrae [39].

2.8 Printing fidelity and porosity analysis

Printing fidelity was evaluated on grid structures by comparing the designed geometry [33] with the printed architecture, by measuring extruded filament thickness in relation to nozzle diameter. At least three constructs per formulation were printed to ensure reproducibility of the printing and post-processing steps. Filament diameter, strand uniformity, pore size, and construct thickness were measured from optical images. Theoretical porosity, based on the computer-aided design (CAD), was compared with the evaluated porosity from the printed scaffolds, which was assessed using Fiji software, as illustrated in Fig. 2 and described by prior work [40]. Based on these values, another printing accuracy metric, expressed as printing fidelity was calculated using the formula:

$$Porosity\ fidelity\ (\%) = \frac{Evaluated\ porosity}{Theoretical\ porosity} \times 100 \quad (1)$$

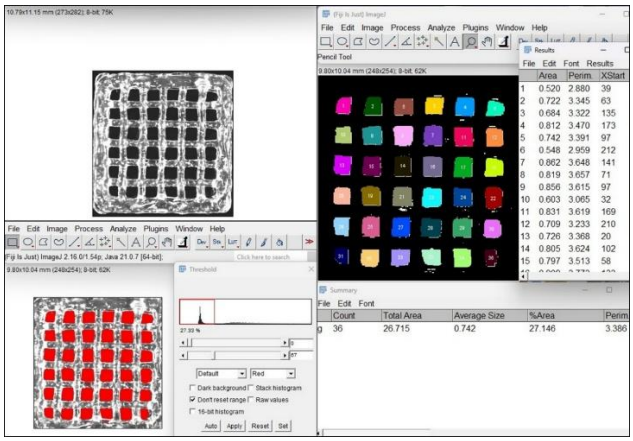


Fig. 2. Porosity evaluation of 3D-printed scaffolds by image-based analysis in Fiji. The original top-view images were converted to 8-bit, and segmented using the threshold function to distinguish the pore regions, analysed with the "Analyze Particles" tool to quantify the number of pores, their individual area, and the total pore area fraction (%Area), providing a quantitative estimate of scaffold porosity.

2.9 Swelling and degradation studies

The swelling behaviour of scaffolds P1–P6 was evaluated gravimetrically in phosphate-buffered saline (PBS, pH 7.4) at 37 °C. Dried scaffolds (W_0) were weighed and then immersed in PBS 1×. After 1 h, samples were gently blotted to remove surface liquid and weighed in the swollen state (W_t). The swelling rate was calculated according to the formula:

$$Swelling\ rate\ (\%) = \frac{W_t - W_0}{W_0} \times 100 \quad (2)$$

where W_t is the scaffold mass at time t and W_0 is the initial dry mass. *In vitro* degradation of scaffolds P1–P6 was assessed gravimetrically by monitoring mass loss in PBS 1× (pH 7.4) at 37 °C for 30 days. At predetermined time points (1, 7, 14, 21, and 30 days), samples were removed from the medium and wiped briefly to eliminate residual fluid prior to weighing.

2.10 MC3T3-E1 Cell culture

MC3T3-E1 preosteoblastic cells [41] were cultured in α-MEM supplemented with 10 % foetal bovine serum, 1 % *L*-glutamine, and 1 % penicillin-streptomycin, under standard culture conditions (37 °C, 5 % CO_2, 90 % humidity). The samples were sterilized by UV-C exposure for 1 h on each side. Cells were seeded directly onto the scaffolds at a density of 100,000 cells/100 µL/sample in 24-well plates and incubated for 30 min to allow initial attachment. Subsequently, the culture medium was brought to a final volume of 1 mL per well, and the samples were further incubated under standard culture conditions for 48 h. The negative control consisted of cells cultured only in complete medium.

2.11 LDH assay

LDH release was used as an indirect indicator of cell membrane damage after contact with the biomaterials. After the incubation period, 50 µL of supernatant from each well were transferred to a new 96-well plate and analysed using the CyQUANT LDH Cytotoxicity Assay (Invitrogen, Thermo Fisher Scientific, Waltham, MA, USA), according to the manufacturer's instructions. After incubation with the assay reagents, absorbance was measured at 490 nm. LDH release was expressed relative to the negative control, represented by cells cultured in the absence of biomaterial.

2.12. Cell fixation for SEM imaging

After incubation, the culture medium was removed, the samples were washed with PBS 1× and fixed in 2.5 % glutaraldehyde for 1 h. The samples were then washed with PBS and dehydrated through graded ethanol solutions (70–100 %) for 30 min at each concentration, followed by incubation with HMDS:ethanol mixtures at 50:50, 75:25, and 100 % HMDS. Prior to imaging, the scaffolds were sputter-coated with a thin gold layer and examined using a FEI Quanta Inspect F50 scanning electron microscope (FEI Company, Hillsboro, OR, USA).

2.13 Statistical analysis

All experiments were performed in replicates, and he results were expressed as *mean* ± *standard deviation* (*SD*). Statistical analysis was performed using Student's t-test and differences were considered statistically significant at $p < 0.05$, $p < 0.01$, and $p < 0.001$. Plots were processed and generated using OriginPro 8.5 (OriginLab Corporation, Northampton, MA, USA) [42].

3. Results

3.1 SiO_2 powder characterization

3.1.1 Thermal analysis

The TG curve of SiO_2 2:1 uncalcined powder (Fig. 3. A) reveals a continuous mass loss from ~100 % to approximately 45 % across the 30–900 °C temperature range, representing a total mass loss of ~55 %, which reflects the high organic content (residual CTAB template) present in the as-synthesised sample. Three distinct decomposition stages are resolved by the DTG and DSC traces. The first event, located at 80–120 °C, is associated with a broad endothermic DSC signal and a DTG peak in the same region, corresponding to the desorption of physiosorbed water and loosely bound surface hydroxyl groups. The dominant decomposition event occurs in the range 200–350 °C, where the DTG curve exhibits two closely spaced sharp peaks at ~280 °C and ~330 °C, accompanied by a pronounced exothermic DSC signal in the same region; this stage corresponds to the oxidative combustion and decomposition of the CTAB surfactant template trapped within the mesopore channels, consistent with the known thermal decomposition range of CTAB in SiO_2 matrices (200–400 °C). A third, gradual mass loss continues from 400 °C to 900 °C without a distinct DTG peak, attributable to the progressive condensation of residual silanol (Si–OH) groups and elimination of structural water, a process characteristic of amorphous SiO_2 densification.

The TG/DTG/DSC profile of SiO_2 4:1 uncalcined powder (Fig. 3. B) closely mirrors that of SiO_2 2:1 in its overall thermal decomposition pattern, with three analogous stages identifiable: initial water desorption below ~150 °C, a principal CTAB combustion event in the range 200–350 °C resolved into two DTG peaks at ~270 °C and ~310 °C with accompanying exothermic DSC features, and a slow silanol condensation regime extending to 900 °C. A notable additional feature in SiO_2 4:1 is the presence of a small but distinct DSC event located at 680–700 °C, which is absent in the SiO_2 2:1 trace and may be associated with a minor structural rearrangement or localised crystallisation event within the amorphous SiO_2 network. The total mass retained at 900 °C (~43 %) is marginally lower than for SiO_2 2:1 (~45 %), suggesting a slightly higher overall organic content or a greater proportion of loosely condensed SiO_2 in the 4:1 precursor ratio.

The overlay of the two TG curves (Fig. 5) confirms that both formulations follow a broadly similar thermal decomposition profile, with the major mass loss event occurring between 200 °C and 350 °C in both cases. The two curves are nearly superimposable up to approximately 250 °C, after which the SiO_2 4:1 sample displays a slightly greater mass loss than SiO_2 2:1 through the 300–400 °C range, despite its lower nominal CTAB content. This behaviour may reflect differences in the removal of loosely bound organics during the washing step rather than intrinsic variations in the surfactant loading. Both samples reach a stable residual mass plateau above 700 °C, confirming that thermal treatment at 550 °C applied during calcination is sufficient to remove the bulk of the CTAB template and yield a predominantly silanol-rich amorphous SiO_2 framework in both cases, required for efficient loading of the bioactive extract. Higher calcination temperatures were deliberately avoided in order to limit the formation of crystalline SiO_2 phases.

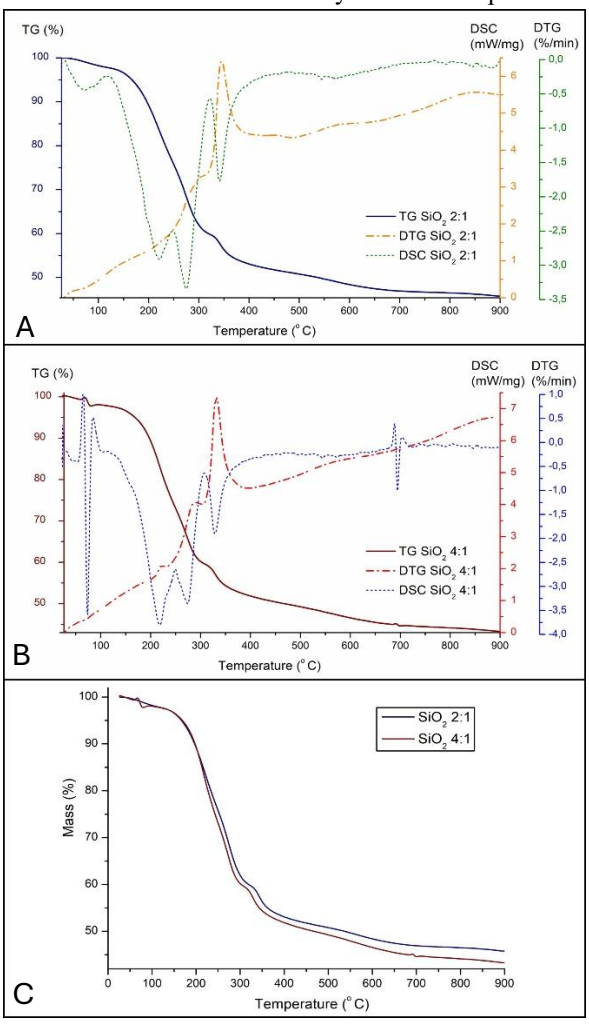


Fig. 3. Simultaneous TG/DTG/DSC analysis and comparative TG profiles of uncalcined SiO_2 powders. (A) SiO_2 2:1 and (B) SiO_2 4:1 measured under air atmosphere from 30 to 900 °C at 10 °C/min. TG (solid line, left axis): mass loss (%); DTG (dotted line, right axis): derivative mass loss rate (%/min); DSC (dashed line, right axis): heat flow (mW/mg). (C) Comparative TG overlay of SiO_2 2:1 (blue) and SiO_2 4:1 (red).

3.1.2 Fourier transformed infrared spectroscopy

FTIR spectra of the as-synthesised SiO_2 2:1 and SiO_2 4:1 powders, illustrated in Fig. 6, show the characteristic vibrations of an amorphous SiO_2 network together with

bands assigned to the CTAB surfactant template. In all spectra, the intense broad band centred at ~1080 cm^{-1} is attributed to the asymmetric stretching of Si–O–Si bonds, while the bands at ~800 cm^{-1} and ~460 cm^{-1} correspond to symmetric Si–O–Si stretching and Si–O–Si bending modes, confirming formation of a typical SiO_2 framework. A shoulder at 950–970 cm^{-1} is assigned to Si–OH stretching vibrations of surface silanol groups, whereas the bands at 2850–2920 cm^{-1} (and the weaker features near ~1470 cm^{-1}) arise from C–H stretching and bending modes of the CTAB alkyl chains trapped within the mesopores.

After calcination at 550 °C, the spectra of SiO_2 2:1 and SiO_2 4:1 samples retain the dominant Si–O–Si bands at ~1080 cm^{-1}, ~800 cm^{-1} and ~460 cm^{-1}, confirming that the SiO_2 network remains intact, but the C–H stretching bands in the 2850–2920 cm^{-1} region are reduced, indicating significant removal of the CTAB template from both materials. Additionally, the Si–OH band around 950–970 cm^{-1} decreases in intensity, reflecting progressive condensation of surface silanols into Si–O–Si bonds during thermal treatment and the corresponding densification of the pore walls.

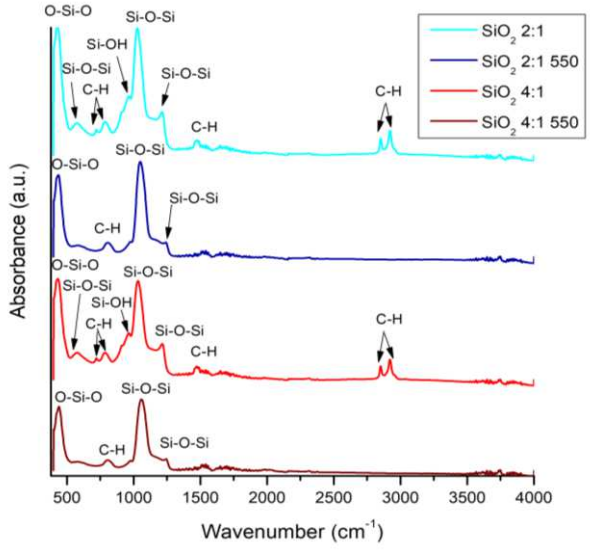


Fig. 4. FTIR spectra of the SiO_2 powders before and after calcination at 550 °C.

3.1.3 X-ray diffraction and energy dispersive X-ray spectrometry

The XRD patterns of both SiO_2 powders calcined at 550 °C, present in Fig. 5. A, exhibit the hallmark combination of an amorphous SiO_2 background and incipient crystalline features. The dominant spectral feature in both samples is a broad, asymmetric halo centred at $2\theta = 22–25$ °, the diagnostic scattering signature of the amorphous SiO_2 network arising from short-range Si–O–Si tetrahedral ordering without long-range periodicity, confirming that the bulk of both materials remains in the amorphous glassy state after calcination at 550 °C, consistent with the known crystallisation threshold of sol-gel SiO_2 [43], which typically converts to cristobalite above 700–800 °C. Superimposed on this background, both samples display two sharp, low-intensity reflections at $2\theta \approx 44$ ° and $2\theta \approx 64$ °, indexed to the (2 0 2) and (2 0 4) planes of β-cristobalite (cubic $Fd\bar{3}m$ space group, ICDD PDF-2 card 01-076-0934), indicating localised structural ordering likely facilitated by residual surface hydroxyl condensation during thermal treatment [44]. In addition, the EDS spectra (Fig. 5. B) confirmed that both TEOS:CTAB = 2:1 and 4:1 SiO_2 powders calcined at 550 °C consist predominantly of silicon (Si $K\alpha$ and $K\beta$)) and oxygen (Si $K\alpha$), with only minor carbon contributions attributed to residual organics and carbon double-sided adhesive tape and gold sputtering to improve sample conductivity used for SEM imaging.

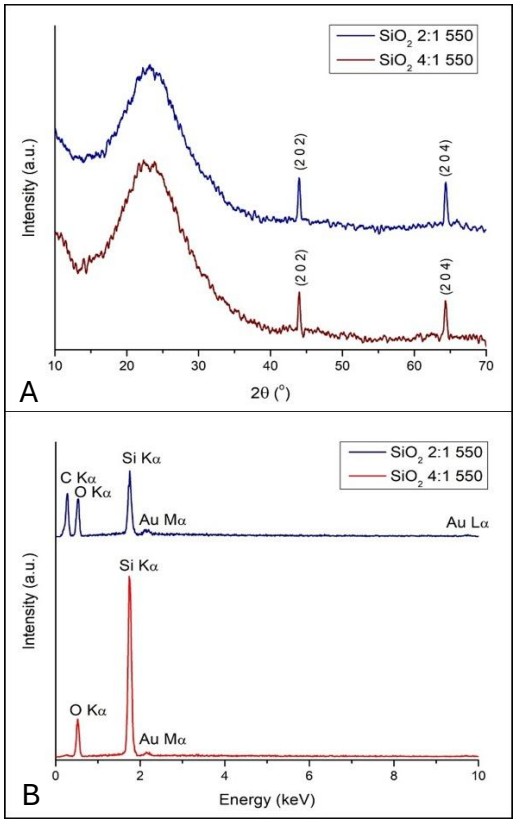


Fig. 5. XRD patterns of SiO_2 calcined powders and EDS spectra of SiO_2 powders, after calcination at 550 °C. (A) Overlapped XRD diffractograms of SiO_2 2:1 (blue line) and SiO_2 4:1 (red line). (B) EDS spectra showing the elemental composition of the SiO_2 2:1 (blue line) and SiO_2 4:1 (red line).

3.1.4 Scanning electron microscopy

SEM analysis of the SiO_2 2:1 calcined sample (Fig. 6. A, B) revealed a powder with a notably broad particle size distribution. At low magnification (10,000×), the particles form a heterogeneous landscape of loosely packed individual spheres interspersed with denser cluster-like aggregates of smaller sub-particles, suggesting a greater tendency toward secondary agglomeration in this composition. At high magnification

(100,000×), measurements confirm individual particle diameters ranging from 360 nm to 620 nm, with the larger particles displaying smooth, lobulated surfaces and the smaller satellites adhering to their surfaces via van der Waals interactions [45]. The slightly broader size polydispersity observed for the SiO_2 2:1 sample compared with SiO_2 4:1 may be related to its faster gelation kinetics during synthesis, which could enable nucleation and growth of a wider range of particle sizes, including larger primary particles alongside smaller nuclei.

SEM analysis of the SiO_2 4:1 calcined sample (Fig. 6. C, D) revealed a densely packed powder composed of predominantly spherical to irregular nanoparticles with a broad size distribution. At low magnification (10,000×), the particles appear closely aggregated into a continuous granular layer with no evidence of large agglomerate clusters or phase separation, indicating homogeneous dispersion within the synthesised batch. At high magnification (100,000×), individual particles display smooth, well-defined curved surfaces with occasional surface roughness, and are observed in point-contact arrangements characteristic of weakly aggregated SiO_2 powders. The particle diameter in this formulation averages 400–700 nm, consistent with the expected size range for sol-gel derived mesoporous SiO_2.

Comparing the two compositions, the SiO_2 4:1 sample exhibited a tighter packing and irregular nanoparticle formation, while the SiO_2 2:1 sample displayed greater polydispersity and a more pronounced clustering tendency. These morphological differences are expected to influence the surface area available for polyphenol adsorption and the tortuosity of the diffusion path within the composite scaffold network, with the more homogeneous 2:1 particles likely providing a more uniform pore-filling effect when incorporated into the Alg/Gel/XG matrix.

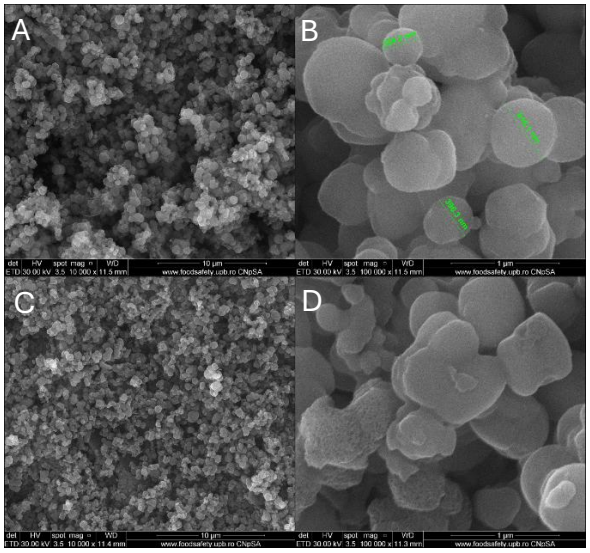


Fig. 6. SEM micrographs of SiO_2 calcined powders. (A, B) SiO_2 2:1 and (C, D) SiO_2 4:1 powder. Left column: overview at 10 000× (scale bar = 10 μm), right column: higher-magnification view at 100 000× (scale bar = 1 μm).

3.1.5 Porosity analysis

The nitrogen adsorption–desorption isotherm of SiO_2 2:1 sample (Fig. 7. A) exhibits a type IV profile with a well-defined hysteresis loop, confirming a well-developed mesoporous architecture [46]. The sample displays a steep uptake and a high total adsorbed volume of 1.06 cm^3/g at $P/P_0 = 0.99$, indicating a greater total pore volume and BET surface area. The BJH pore size distribution curve reveals a sharp, intense peak centred at 3.5–4.0 nm pore width (W), confirming a large mesopore volume concentrated within a narrow size range. This behaviour is consistent with the lower TEOS:CTAB ratio used for the 2:1 material, since a higher surfactant content promotes the formation of more ordered micellar templates [47] and typically increases accessible surface area and pore volume in CTAB-templated mesoporous SiO_2. The resulting textural properties are particularly favourable for polyphenol loading and sustained diffusion-controlled release, as the pore dimensions are commensurate with the molecular sizes of resveratrol, catechin, and related phenolic acids.

The nitrogen adsorption–desorption isotherm of SiO_2 4:1 sample (Fig. 12) also displays a type IV profile with a narrow hysteresis loop in the P/P_0 range of 0.45-0.65, characteristic of capillary condensation in uniform mesopores and confirming the mesoporous nature of the material. The steep uptake at very low relative pressures ($P/P_0 < 0.05$) indicates a significant microporous contribution arising from the textural porosity of the nanoparticle aggregates [45], while the gradual increase at $P/P_0 > 0.8$ without reaching a plateau reflects multilayer adsorption on external particle surfaces and interparticle void filling, consistent with the packed morphology observed by SEM. The BJH pore size distribution shows that both materials share the same mean mesopore diameter, but a peak $dV/dlog(W)$ of ~11 cm^3/g and a total adsorbed volume of 0.92 cm^3/g at P/P_0=0.99, which confirms a narrow, unimodal mesopore distribution but with a lower mesopore volume than SiO_2 2:1. This reduction in surface area and total pore volume is in agreement with the higher TEOS:CTAB ratio used for the 4:1 situation, since a lower surfactant fraction generally leads to thicker SiO_2 walls and fewer well-defined micellar domains, thereby decreasing the overall mesopore volume in CTAB-templated SiO_2 networks.

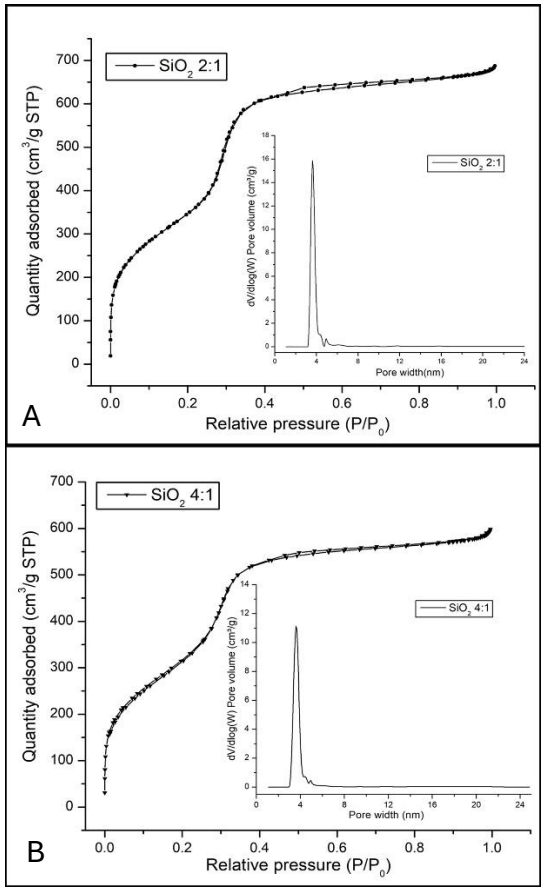


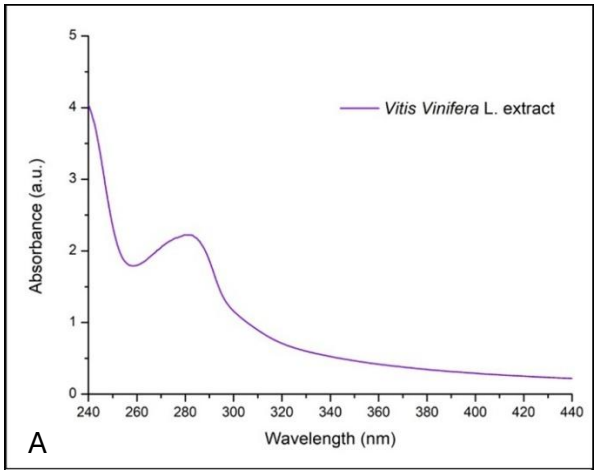
Fig. 7. Nitrogen adsorption–desorption isotherm of SiO_2 calcined powders. (A) SiO_2 2:1, (B) SiO_2 4:1; insets: BJH pore size distribution derived from the desorption branch, showing differential pore volume as a function of pore width (*dV/dlog(W)*).

3.1.5 Release profile via UV-Vis spectrometry

The UV–Vis spectrum of the free *Vitis vinifera* L. Soxhlet extract (Fig. 8. A) exhibited a broad, intense absorption onset below 260 nm and a well-defined peak at 280–290 nm, consistent with the characteristic UV fingerprint of a complex grape polyphenolic mixture [48]. This absorption band is attributable to the overlapping contributions of the dominant flavanols present in grape peel and seed fractions, most notably (+)-catechin ($\lambda_{max} \approx$ 280 nm) and (−)-epicatechin ($\lambda_{max} \approx$ 276–278 nm) [6], which are among the most abundant low-molecular-weight polyphenols in *Vitis vinifera* L. pomace. Additional contributions arise from gallic acid ($\lambda_{max} \approx$ 272 nm) [1], protocatechuic acid (227–260 nm), caffeic acid (~217 nm and 295–327 nm) [20], and hydroxycinnamic acid derivatives including caftaric and ferulic acids. Flavonols such as quercetin and myricetin contribute secondary absorption bands (Band II) in the 250–280 nm window and primary bands (Band I) in the range 330–385 nm. The absence of a visually distinct isolated peak at 305–310 nm does not exclude the presence of *trans*-resveratrol; rather, it reflects the fact that resveratrol characteristic λ_{max} (≈ 305–308 nm for *trans*-, ≈ 286–288 nm for *cis*-) is masked by the more intense 280 nm band of the flavanol and phenolic acid fraction [49], which typically predominates by at least one order of magnitude in bulk grape extracts.

The UV–Vis spectra shown in Fig. 8. B were recorded on the residual supernatant collected after loading and recovery of the SiO_2 nanoparticles by filtration, on the fraction of the grape peel extract that was not adsorbed onto the carrier. Both spectra retain the characteristic absorption peak at 280–290 nm, confirming the presence of polyphenolic chromophores in both filtrates. Notably, the SiO_2 2:1 filtrate displays lower absorbance values across the entire measured range compared with SiO_2 4:1, indicating that a greater proportion of the polyphenolic constituents was removed from solution by the 2:1 carrier, which is consistent with its higher specific surface area and total pore volume providing a larger number of accessible adsorption sites and stronger silanol–polyphenol interactions. Conversely, the higher residual absorbance of the SiO_2 4:1 filtrate reflects the comparatively lower uptake capacity of this formulation. The sloping, non-zero absorbance baseline extending from 320 nm toward 440 nm is attributed to Mie scattering from fine SiO_2 nanoparticles that passed through the filter paper owing to their sub-micrometre dimensions, decaying monotonically with increasing wavelength.

A broadening of the spectral shoulder toward 295–315 nm is discernible in both loaded SiO_2 spectra, where *trans*-resveratrol ($\lambda_{max} \approx$ 305–308 nm) and any *cis*-resveratrol formed by photo-induced isomerisation during handling ($\lambda_{max} \approx$ 286–288 nm) are expected to contribute. A slight bathochromic shift of 1–3 nm and a decrease in peak intensity relative to the free extract are indicative of successful polyphenol adsorption within the SiO_2 pores, and may reflect hydrogen bonding or π–π interactions between the hydroxyl groups of the polyphenols and surface silanol groups.



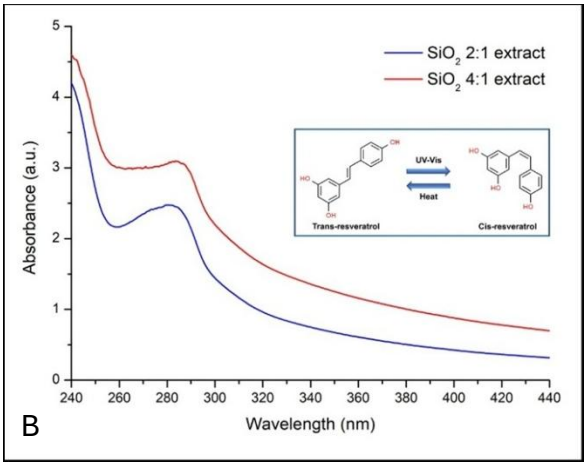


Fig. 8. UV–Vis absorption spectra of *Vitis vinifera* L. grape extract and residual supernatants after SiO_2 loading. (A) Absorption spectrum of the Soxhlet-derived *Vitis vinifera* L. extract recorded between 240 and 440 nm. (B) UV–Vis spectra of the residual supernatants collected after loading and filtration of SiO_2 2:1 (red line) and SiO_2 4:1 (blue line). The inset illustrates the reversible photoisomerisation equilibrium between the biologically active *trans*-resveratrol and the less active *cis*-resveratrol forms.

3.2 Rheological evaluation of the hydrogels

Rheological characterisation was performed on selected formulations: hydrogel inks P1 and P4, and composite ink P3 (containing 2 wt% SiO_2 2:1). Direct rheological testing of SiO_2-containing composite inks was not feasible, as the abrasive nature of the SiO_2 particles poses a risk of damage to the stainless-steel parallel-plate geometry. Preliminary evaluation of P1 and P4, which differ only in gelatine content (6 wt% vs. 8 wt%), revealed no statistically significant differences in viscoelastic behaviour attributable to this compositional variation alone. Therefore, the rheological results of P4 are presented as representative of the hydrogel matrix behaviour.

The amplitude sweep (Fig. 9. A), conducted over a strain range of 10^{-4} to 10^{1} at a fixed angular frequency of 1 s^{-1}, revealed a well-defined linear viscoelastic region (*LVE*) with a plateau storage modulus $G' \approx$ 1,200-1,300 Pa and loss modulus $G'' \approx$ 200-220 Pa, confirming a strongly elastic-dominant gel network. The yield point was identified at 0.05 – 0.10 strain, where G' began to decline, while the gel-to-fluid transition occurred at 1–2, consistent with a physically cross-linked network susceptible to progressive structural breakdown under increasing deformation.

The frequency sweep (Fig. 9. B), performed within the *LVE* at a constant strain of 0.001 over an angular frequency range of 0.05–100 s^{-1}, confirmed the gel-dominated character of the hydrogel across all probed timescales, with G' exceeding G'' throughout and no terminal relaxation crossover observed. The storage modulus increased moderately from ~1000 Pa to ~2000 Pa over three decades of frequency, while the loss modulus rose from ~150 Pa to ~800 Pa, a mild frequency dependence. The complex viscosity η^* decreased from ~25000 Pa·s at 0.05 s^{-1} to ~20 Pa·s at 100 s^{-1} following a power-law trend.

The steady-shear flow curve (Fig. 9. C), acquired over a shear rate range of ~3×10^{-3} s^{-1} to 3 s^{-1}, showed pronounced shear-thinning behaviour, with apparent viscosity decreasing by approximately two orders of magnitude across the measured window, consistent with a power-law fluid with flow index $n < 1$. A slight levelling of viscosity at the lowest shear rates is suggestive of a yield stress or near-Newtonian plateau.

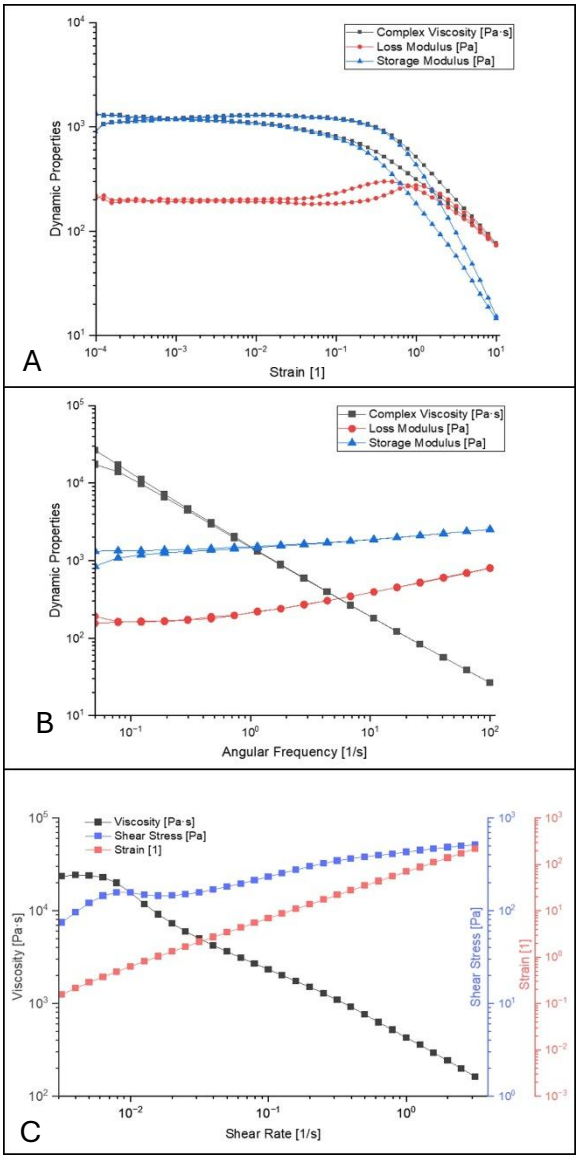


Fig. 9. Rheological characterisation of Alg/Gel/XG hydrogel ink (P4) at 25 °C. (A) Amplitude sweep: storage modulus (G', blue triangle line), loss modulus (G'', red dotted line), and complex viscosity (η^*, black square line) recorded at a fixed angular frequency of 1 s^{-1} as a function of strain amplitude, used to determine the linear viscoelastic region (LVR). (B) Frequency sweep within the LVR: G', G'', and η^* measured at a constant strain of 0.001 over an angular frequency range of

0.05–100 s^{-1}. (C) Steady-shear flow curve: apparent viscosity (black curve), shear stress (blue curve), and strain (red curve) as a function of shear rate (3×10^{-3}–3 s^{-1}), illustrating the shear-thinning behaviour of the ink.

Taken together, the three measurements delineate a rheological profile with high elastic modulus at rest, a well-defined yield point, and steep shear-thinning behaviour. The frequency sweep further reveals a crossover of G' and G'' at high angular frequencies (10–10^2 s^{-1}), indicating a transition from gel-dominant to more liquid-like behaviour under rapid oscillatory deformation, consistent with the dynamic conditions experienced by the ink during extrusion through the nozzle. This profile is characteristic of inks suitable for pneumatic extrusion-based 3D printing, where the material must flow readily under nozzle-imposed shear and rapidly recover its elastic-dominant structure upon deposition to maintain filament shape and ensure dimensional fidelity of the printed construct.

3.3 3D-printed scaffolds evaluation

3.3.1 Visual aspect of the 3D-printed scaffolds

All six formulations (P1–P6) were successfully extruded and printed into 3D constructs (Fig. 10), confirming the printability of both the Alg/Gel/XG and composite inks across the tested compositions. Visually, the hydrogel-only scaffolds (P1, P4) appeared as translucent, slightly opalescent structures, with a uniform off-white colour attributable to the hydrogel matrix. Upon incorporation of SiO_2 (P2, P3, P5, P6), the scaffolds acquired a progressively opaquer, matte-white appearance consistent with the light scattering from the dispersed inorganic particles, with the effect becoming more pronounced at higher SiO_2 loading (2 wt% vs. 0.5 wt%).

The pristine hydrogel formulations P1 and P4 exhibited progressive collapse under their own weight during multi-layer deposition, resulting in flattened constructs with poorly defined gyroid morphology and compressed inter-layer spacing. This behaviour is consistent with the rheological profile of the hydrogel ink: the slow structural recovery following yield, evidenced by the gradual G' decline beyond the crossover, further limits the ability of the hydrogel to support overlying layers before crosslinking is achieved. In contrast, the composite cylindrical scaffolds (P2, P3, P5, P6) maintained their target height and lateral dimensions after deposition, with the gyroid infill pattern remaining discernible, confirming that even low SiO_2 loadings are sufficient to confer the post-deposition rigidity required for stable multi-layer cylindrical fabrication.

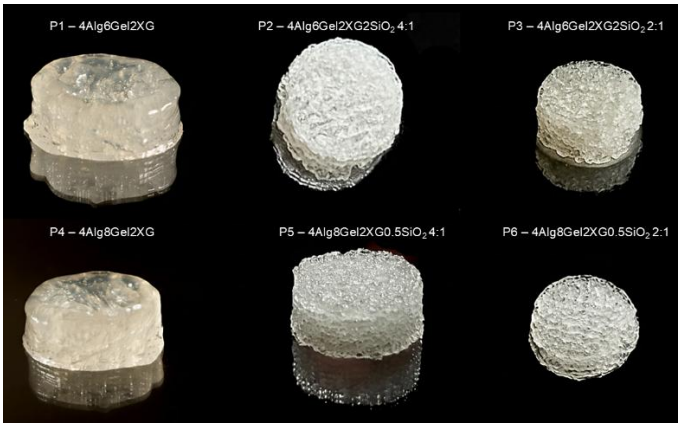


Fig. 10. Macroscopic appearance and printing quality of the 3D-printed scaffolds P1-P6 before crosslinking.

3.3.2 Fourier transform infrared spectroscopy and energy-dispersive X-ray spectroscopy

For the crosslinked scaffolds, the FTIR spectra illustrated in Fig. 11. A, confirms the simultaneous presence of the Alg/Gel/XG polymer network and the SiO_2 phase, as well as their interactions. In all formulations (P1–P6), the broad band centred at 3300–3400 cm^{-1} is assigned to O–H stretching of hydroxyl and carboxyl groups from the polysaccharides and bound water in the hydrogel matrix. The bands near 2920–2850 cm^{-1} arise from aliphatic C–H stretching of the polysaccharide and protein backbones. In the 1700–1500 cm^{-1} region, the peak at 1630–1650 cm^{-1} (amide I, C=O stretching) and the band at 1540–1550 cm^{-1} (amide II, C–N stretching/N–H bending) are characteristic of gelatine peptide bonds and confirm the protein component of the composite. In the same region, shoulders or additional contributions at 1590–1610 cm^{-1} and 1400–1420 cm^{-1} can be attributed to asymmetric and symmetric stretching of alginate carboxylate groups (COO^-), consistent with Ca^{2+}/polymer ionic crosslinking and electrostatic interactions between alginate and gelatine.

At lower wavenumbers (1200–900 cm^{-1}), all spectra show intense bands assigned to C–O–C and C–O stretching vibrations of the glycosidic bonds and saccharide ring of alginate and xanthan gum, confirming that the polysaccharide backbone remains intact after scaffold fabrication. In the SiO_2-containing scaffolds (P2, P3, P5, P6), these polysaccharide bands are complemented by Si–O–Si stretching vibrations of the embedded SiO_2 phase, typically observed as strong absorptions in the 1050–1100 cm^{-1} region with associated bands near 800 and 460 cm^{-1}. The increased intensity and slight broadening of the Si–O–Si band in these formulations relative to P1 (polymer-only) indicate successful incorporation and dispersion of SiO_2 within the hydrogel matrix, while the preservation of characteristic polysaccharide and amide bands across P1–P6 demonstrates that the organic network remains chemically

intact, supporting the structural integrity and biofunctionality of the composite scaffolds.

The EDS spectra of scaffolds P1–P6 (Fig. 11. B) confirm the expected organic–inorganic composition of the alginate–gelatin–xanthan gum/$CaCl_2$/SiO_2 system. All samples display prominent carbon (C *Kα*) and oxygen (O *Kα*) peaks, together with nitrogen (N *Kα*), reflecting the polysaccharide–protein matrix, while sodium (Na *Kα*) is attributed to sodium alginate and calcium (Ca *Kα* and *Kβ*) / chlorine (Cl *Kα* and *Kβ*) arise from $CaCl_2$-mediated ionic crosslinking of alginate chains. A small aluminium (Al *Kα*) signal likely originates from the aluminium SEM sample stub, and the gold (Au *Lα*) peak observed at higher energies corresponds to the thin gold coating applied for the SEM analysis.

The key compositional difference between formulations is the presence of silicon (Si): no Si peak is detected for the polymer-only scaffolds P1 and P4, whereas clear Si *Kα* (and in some cases Si *Kβ*) peaks appear for P2, P3, P5, and P6, confirming successful incorporation of the mesoporous SiO_2 phase in these composite scaffolds. The comparable Ca and Cl peak intensities across all spectra indicate similar levels of ionic crosslinking, while the additional Si signal in P2, P3, P5, and P6 verifies that the inorganic filler is well retained within the printed constructs and not removed during gelation, washing, or drying steps.

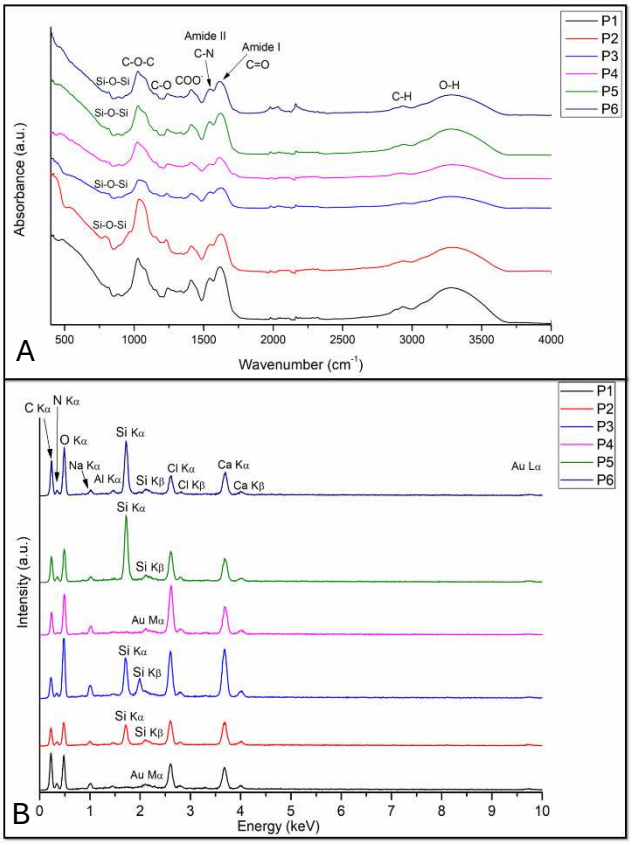


Fig. 11. Chemical and structural characterization of the 3D-printed scaffolds P1–P6. (A) Overlapped FTIR spectra and (B) elemental composition illustrated by EDS spectra.

3.3.3 Scanning electron microscopy

SEM examination of P1 scaffold at low magnification (Fig. 12. A) revealed a layered filament structure with a homogeneous, single-phase appearance and partially compressed inter-layer spacing, consistent with the limited post-deposition shape retention observed macroscopically for the pristine hydrogel formulation. At higher magnification (Fig. 12. B), the filament surface appeared smooth and continuous, with no visible particulate inclusions, confirming the absence of an inorganic phase and the uniform character of the unmodified Alg/Gel/XG matrix.

The P2 composite scaffold (2.0 wt% SiO_2 4:1), shown in Fig. 12. C, D, displayed improved filament definition at low magnification relative to P1, with more regular inter-layer spacing and better-preserved gyroid pore geometry, reflecting the dimensional reinforcement conferred by the incorporated SiO_2 phase. At higher magnification, the filament surface exhibited a noticeably rougher and more textured morphology compared with the hydrogel-only scaffolds, with bright submicrometric features distributed across the polymer matrix corresponding to SiO_2 4:1 particles embedded within the biopolymer network. The absence of large agglomerates or localised SiO_2-rich domains suggests adequate dispersion of the inorganic phase at 2 wt% loading. At low magnification, the P3 scaffold (2 wt% SiO_2 2:1, Fig. 12. E, F) showed well-defined continuos filmanet formation, consistent with the greater reinforcing capacity of the more mesoporous SiO_2 2:1 sample. The higher-magnification image revealed the densest distribution of SiO_2 inclusions across the filament surface among all six formulations, with the surface roughness being more pronounced than in P2. This difference is attributable to the distinct particle morphology and higher specific surface area of the SiO_2 2:1 phase relative to SiO_2 4:1, which may promote stronger interfacial interactions with the surrounding biopolymer matrix.

The P4 scaffold (Fig. 13. A, B), comprising the higher-gelatine hydrogel without SiO_2 (8 % gelatine vs. 6 % in P1), presented a similar degree of layer deformation and pore collapse at low magnification as P1, confirming that increasing the gelatine content from 6 % to 8 % alone is insufficient to meaningfully improve post-deposition shape retention in the absence of an inorganic reinforcing phase. At higher magnification, the filament surface was smooth and featureless, morphologically comparable to P1, though with a marginally denser matrix appearance consistent with the higher gelatine concentration contributing to a more compact crosslinked network.

Despite containing only 0.5 wt% SiO_2 4:1, the P5 scaffold (Fig. 13. C, D) exhibited noticeably improved filament regularity and pore definition at low magnification compared with the hydrogel-only P4

scaffold, demonstrating that even sub-percent SiO_2 incorporation is sufficient to enhance dimensional fidelity during printing. At higher magnification, sparse but uniformly distributed bright SiO_2 features were visible on the filament surface, producing an intermediate surface texture between the smooth P4 matrix and the more densely particle-covered P2 surface. The homogeneous spatial distribution of these inclusions at low loading further supports the effectiveness of the dispersion protocol in preventing SiO_2 sedimentation or aggregation within the ink.

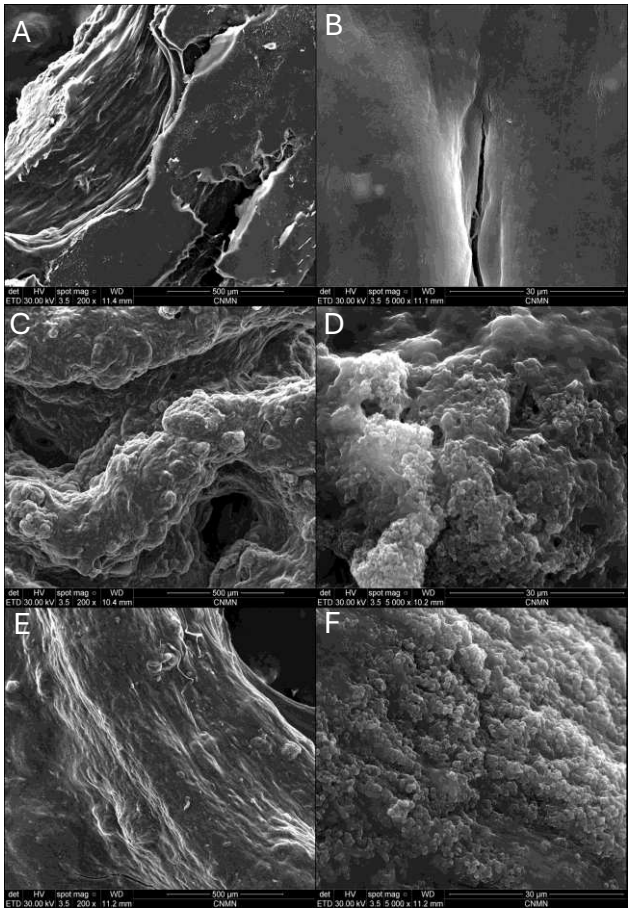


Fig. 12. SEM micrographs of the 3D-printeds scaffolds. (A, B) P1 pristine hydrogel scaffold, (C, D) P2 composite scaffold - 0.5 wt% SiO_2 4:1 and (E, F) P3 composite scaffold - 0.5 wt% SiO_2 2:1. Top row: morphology at 200× (scale bar = 500 µm) and bottom row: higher-magnification view at 5000× (scale bar = 30 µm).

The P6 scaffold (0.5 wt% SiO_2 2:1) showed a macroscopic appearance at low magnification (Fig. 13. E) comparable to P5, with well-preserved pore channels and defined layer boundaries, confirming adequate printability and shape retention at this loading level. At higher magnification (Fig. 13. F), the filament surface displayed a finely textured morphology with sparsely distributed SiO_2 2:1 inclusions, subtly different in particle distribution pattern from P5, which is attributable to the distinct mesopore architecture and surface chemistry of the 2:1 SiO_2 relative to the 4:1 SiO_2. No evidence of interfacial debonding, particle clustering, or matrix discontinuity was observed, confirming the structural integrity of the composite at low SiO_2 content.

In all formulations, occasional micro- and macro-cracks were observed within individual filaments and along filament–filament interfaces, particularly in polymer-rich regions. These fissures are most likely associated with drying and sample preparation for SEM, including exposure to high vacuum, which are known to induce desiccation shrinkage, and subsequent cracking in highly hydrated alginate- and gelatine-based hydrogels rather than reflecting true defects in the as-printed scaffolds.

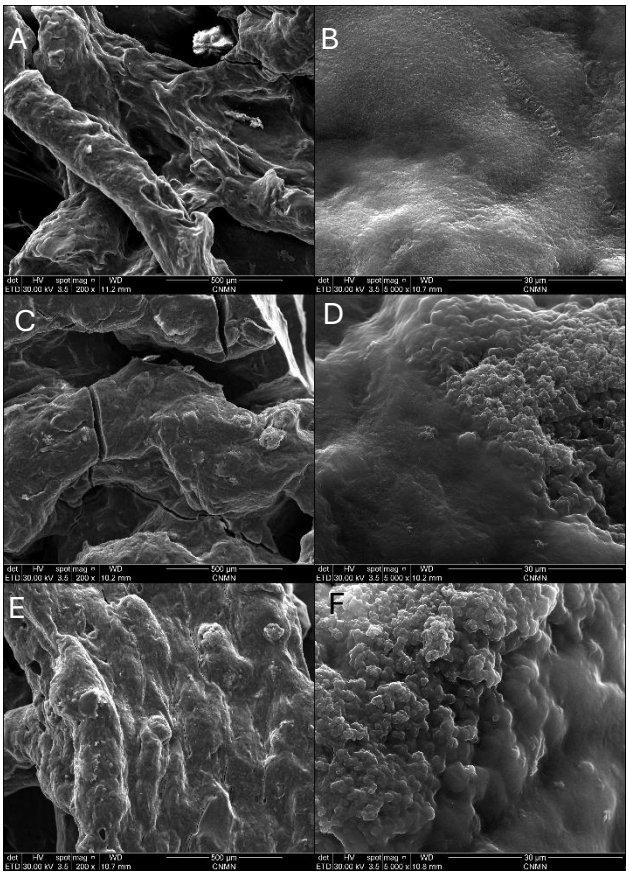


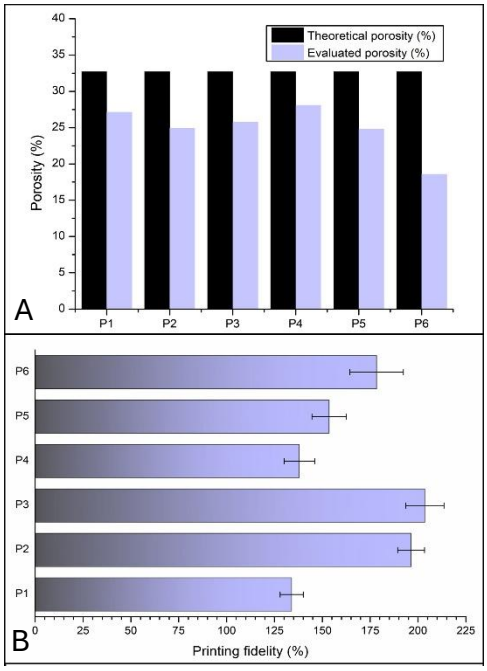
Fig. 13. SEM micrographs of the P6 3D-printed scaffolds. (A, B) P4 pristine hydrogel scaffold, (C, D) P5 composite scaffold - 0.5 wt% SiO_2 4:1 and (E, F) P6 composite scaffold - 0.5 wt% SiO_2 2:1. Top row: morphology at 200× (scale bar = 500 µm) and bottom row: higher-magnification view at 5000× (scale bar = 30 µm).

3.3.4 Printing accuracy evaluation

Filament strand thickness and printing fidelity analysis (Fig. 14. A, B) showed that all six formulations produced extruded filaments with mean strand diameters exceeding the nominal nozzle diameter of 250 µm. This behaviour is characteristic of non-Newtonian viscoelastic hydrogels and is primarily attributed to the die-swell effect: upon exiting the nozzle, the elastic component of the ink partially recovers the deformation imposed during flow, causing radial expansion of the extruded filament

beyond the nozzle diameter. The hydrogel-only formulations P1 and P4 exhibited the greatest die-swell and spreading, with mean strand thicknesses of ~410 µm and ~350 µm respectively, corresponding to printing fidelity values of ~130 % (P1) and ~140 % (P4), consistent with their lower elastic modulus and reduced resistance to post-deposition deformation. The composite formulations P2, P3, P5, and P6 displayed higher absolute strand thicknesses due to their greater total solid content; their printing fidelity values were also consistent, reflecting the increased ink viscosity and yield stress imparted by the SiO_2 phase, which constrains both die-swell magnitude and post-deposition spreading, resulting in more reproducible filament dimensions across successive print passes.

Porosity analysis (Fig. 14. C) confirmed that the experimentally measured porosity of all scaffolds was lower than the theoretical CAD-designed value of ~33 %, indicating that filament spreading and partial pore occlusion, direct consequences of the die-swell and post-deposition flow described above, reduce the open pore area relative to the design target across all compositions. Despite this, the evaluated porosities of P1–P5 remained within a relatively narrow range (24–27 %), suggesting that the scaffold architecture is reasonably well reproduced across most formulations and that all systems retain an open macroporous network compatible with nutrient transport and cell infiltration. P6 was the exception, displaying the lowest evaluated porosity of ~18 %, the greatest deviation from the theoretical target. This may reflect the combined effect of the SiO_2 2:1 phase within the higher-gelatine P6 formulation producing a particularly stiff, dense filament prone to greater lateral spread at the lower extrusion flow rates required for this composition, thereby partially occluding the designed pore spaces.



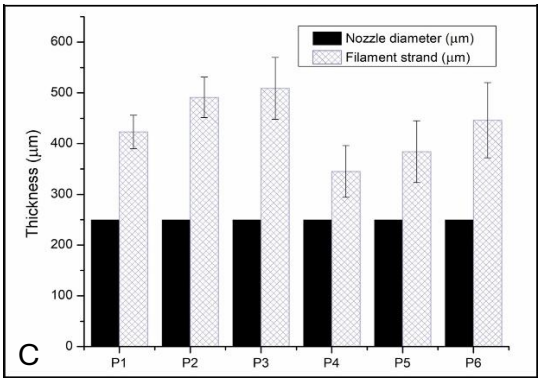


Fig. 14. Printing quality metrics. (A) Accuracy of the 3D extrusion process (bars represent the mean strand thickness for each nozzle diameter used), and (B) Printing fidelity expressed as the ratio between measured filament strand thickness and nominal nozzle diameter, values closer to 100 % reflect high printing fidelity; deviations above or below this value indicate over- or under-extrusion, respectively. (C) Comparison of theoretical and evaluated porosity for scaffolds P1–P6.

3.3.5 Swelling and degradation rate

Swelling analysis of the six scaffold formulations, illustrated in Fig. 15. A, revealed a clear inverse relationship between SiO_2 content and equilibrium water uptake, with P1 recording the highest swelling ratio of ~277 % and P3 the lowest at ~107 %. The hydrogel-only scaffolds P1 exhibited greater water absorption, attributable to their open, purely polymeric network with a higher density of unoccupied hydrophilic chain segments and larger effective pore volume available for water ingress. The systematic reduction in swelling observed across the composite formulations is consistent with the known mechanism by which surface silanol groups (Si–OH) form hydrogen bonds with the hydroxyl and carboxylate groups of alginate and gelatine chains, restricting network chain mobility, and reducing pore volume accessible to water molecules. The particularly low swelling of P3 (SiO_2 2:1, 2 wt%) relative to P2 (SiO_2 4:1, 2.0 wt%) further reflects the higher specific surface area and denser silanol coverage of the 2:1 particles, amplifying the extent of polymer–SiO_2 hydrogen bonding at equivalent loading. Similarly, within the 0.5 wt% group, P6 (SiO_2 2:1, 145.77 %) swells less than P5 (SiO_2 4:1, 187.5 %), reinforcing that particle surface chemistry, not only loading, governs the swelling response.

The degradation profiles over 30 days (Fig. 15. B) showed progressive mass loss in all formulations, consistent with hydrolytic and enzymatic degradation of the polysaccharide and protein components under the test conditions. P4 exhibited the fastest degradation trajectory, approaching 90 % mass loss by day 30, followed by P1 (~75 %), reflecting the limited structural stability of the polymer-only matrices. The composite scaffolds P2, P3, P5, and P6 all degraded more slowly, with final degradation rates converging in the 55–70 % range,

demonstrating that SiO_2 incorporation confers greater resistance to matrix dissolution an effect directly coupled to the increased crosslinking density evidenced by the lower swelling ratios of these formulations, since a denser crosslinked network slows water diffusion and chain disentanglement. The notably faster degradation of P4 relative to P1 despite both being hydrogel-only formulations may reflect the higher gelatine content (8 % vs. 6 %) in P4, as gelatin undergoes faster hydrolytic dissolution than the ionically crosslinked alginate network, particularly under the ion-exchange conditions of PBS. Together, the swelling and degradation data are internally consistent, confirming that SiO_2 phase incorporation effectively slows both water uptake and matrix dissolution, providing a tunable degradation window compatible with the requirements of tissue regeneration scaffolds.

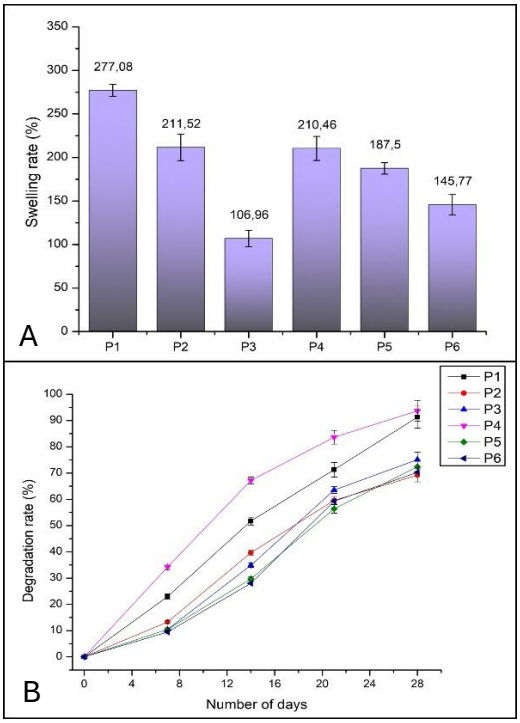


Fig. 15. Swelling and degradation behaviour of 3D-printed scaffolds P1–P6 in PBS 1× (pH 7.4, 37 °C). (A) Equilibrium swelling rate expressed as percentage mass increase (%) after 1 h immersion. (B) Degradation rate (%) as a function of immersion time over 30 days (time points: 1, 7, 14, 21, and 30 days), illustrating the evolution of mass loss for each formulation.

3.3.6 Release profile via UV-Vis spectroscopy

UV–Vis spectra recorded at successive time points (5–180 min) for the composite scaffolds P2 (Fig. 16. A) and P3 (Fig. 16. B) show a progressive, time-dependent increase in absorbance across the 200–450 nm range, consistent with the diffusion of UV-active species from the scaffold matrix into the release medium. The most pronounced changes occur in the deep-UV region, where a broad increase in absorbance indicates the cumulative release of a mixture of low-molecular-weight organic compounds originating from the hydrogel network and, to a lesser extent, the *Vitis Vinifera* L. peel extract (catechin $\lambda_{max} \approx$ 280 nm [17], epicatechin $\lambda_{max} \approx$ 278 nm [50], gallic acid $\lambda_{max} \approx$ 272 nm, caffeic acid, and related hydroxycinnamic acid derivatives, all of which absorb strongly below 240 nm in addition to their characteristic near-UV bands [51]) loaded in the mesoporous SiO_2.

Given the low proportion of extract relative to the total scaffold mass and the complex composition of the Alg/Gel/XG/SiO_2 system, these spectra are interpreted qualitatively as evidence of sustained leaching of multiple organic components, rather than being attributed to individual polyphenols. Moreover, the Alg/Gel/XG scaffold is both ionically and covalently crosslinked and the *Vitis Vinifera* L. extract is confined within mesoporous SiO_2 particles embedded in this network, so the effective diffusion pathway is highly restricted. Substantial extract release is therefore expected to occur over significantly longer times than the 180 min window assessed. Any contribution from resveratrol would be expected in the 300–310 nm range; however, given the predominance of catechins and phenolic acids in the bulk extract and the additional diffusion barrier imposed by the crosslinked hydrogel network, no clearly resolved resveratrol peak emerges above the spectral background within the 180 min observation window.

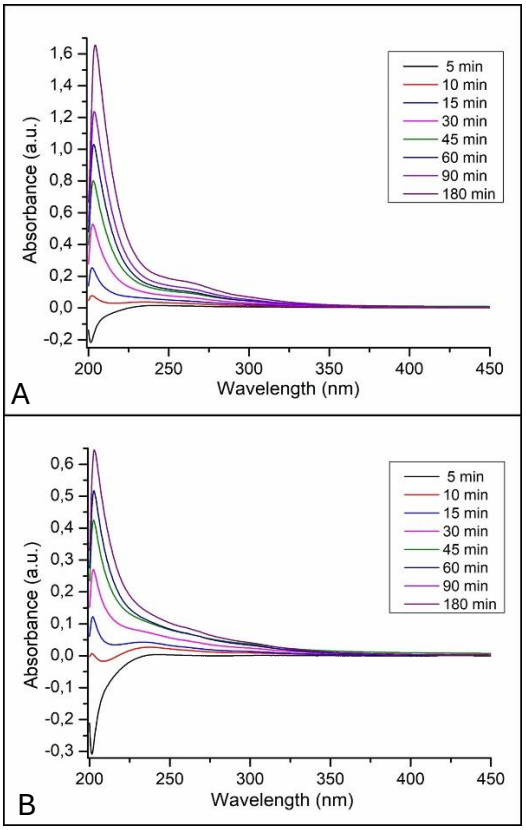


Fig. 16. Time-resolved UV–Vis absorption spectra of compounds released from composite scaffolds. (A) Spectra recorded for the P2 scaffold (2 wt% SiO_2 4:1) at 5–180 min. (B) Corresponding spectra for the P3 scaffold (2 wt% SiO_2

2:1), displaying a higher absolute absorbance but a similar spectral shape.

3.3.7 Biological evaluation

The LDH values for both P5 (0.871 relative to control) and P6 (1.034 relative to control, $p < 0.05$ vs. control) remained close to the negative control, indicating that the cell membrane remained largely intact throughout the 48 h incubation period. The slightly lower LDH value for P5 compared to P6 is also consistent with the somewhat different SiO_2 content and its potential influence on surface properties.

It is important to acknowledge that glutaraldehyde, used at 0.5 wt% during the post-print crosslinking step, is a known cytotoxic agent at elevated concentrations [52]. In this study, constructs were subjected to washing with PBS 1× after crosslinking to remove unreacted glutaraldehyde and excess $CaCl_2$ prior to cell exposure. The observed LDH release values remaining near the negative control baseline suggest that the washing protocol was effective in reducing residual glutaraldehyde to sub-cytotoxic levels. Nevertheless, quantification of residual aldehyde content by colorimetric assay in future work would provide direct evidence of crosslinker removal and strengthen the cytocompatibility interpretation.

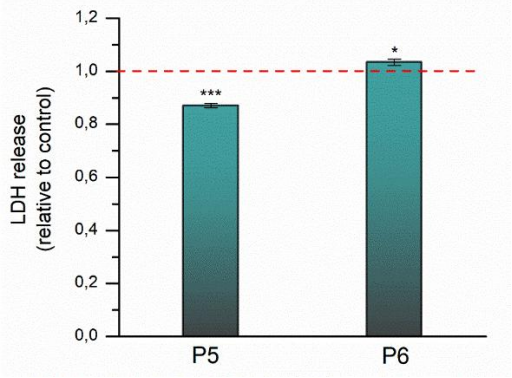


Fig. 17. LDH release of MC3T3-E1 pre-osteoblastic cells after 48 h direct exposure to scaffold, normalised to the negative control.

SEM imaging of scaffolds P5 (Fig. 18. A, B) and P6 (Fig. 18. C, D) after 48 h of direct contact with MC3T3-E1 preosteoblasts revealed the presence of cells and cell aggregates distributed across the scaffold surface and within the interconnected pore regions of both formulations. At lower magnification (300 µm scale), the scaffolds display an irregular, multi-layered surface consistent with the dried hydrogel/SiO_2 composite architecture, with numerous cellular bodies visible in both open pore cavities and on filament surfaces, confirming that the material is capable of supporting initial cell attachment. At higher magnification (50 µm scale), individual and clustered cells appear as compact, roughly spherical bodies, with visible surface texture suggesting partial membrane preservation after chemical fixation and HMDS-based dehydration.

Notably, the cells predominantly displayed an irregular morphology with limited flattening and spreading across the substrate surface in both P5 and P6. This morphological profile is consistent with an early or restricted adhesion state and is commonly observed for MC3T3-E1 cells when cultured on substrates that do not yet provide sufficient integrin-binding sites or optimal surface stiffness for cytoskeletal reorganization and focal adhesion maturation. It has been well documented that MC3T3-E1 pre-osteoblasts initially adopt a round morphology on hydrogel substrates [53], and that transition towards an elongated, spread phenotype requires both appropriate surface chemistry and adequate mechanical cues [54, 55], typically developing over several days rather than within the first 48 h. Surface roughness also plays an important role: MC3T3 cells have been reported to remain rounded on smooth surfaces and elongate preferentially on rougher topographies [56]. Since Alg/Gel/XG hydrogels present a smooth, highly hydrated surface with limited protein adsorption capacity compared with conventional tissue culture plastic, a predominantly rounded cell phenotype at 48 h is not unexpected and does not, in itself, indicate cytotoxicity.

Comparing P5 and P6 directly, both formulations showed qualitatively similar cell distribution patterns in SEM, with no visible large areas of surface completely devoid of cells, though individual cell spreading appears limited in both cases.

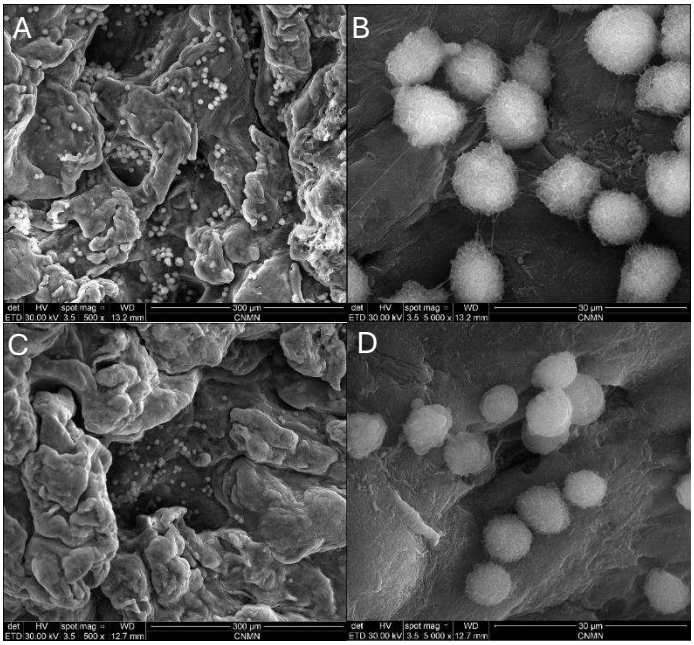


Fig. 18. SEM micrographs of MC3T3-E1 preosteoblastic cells cultured on composite scaffolds for 48 h. (A–B) P5 scaffold and (C–D) P6 scaffold. Left column: overview at 500× (scale bar = 300 µm), right column: higher-magnification view at 5000× (scale bar = 30 µm).

4. Discussion

The present results confirm that combining alginate and gelatine in a 3D printable hydrogel [27] is a robust strategy for fabricating cell-compatible scaffolds [57] with tunable architecture, in agreement with previous work on alginate–gelatine inks for bone regeneration [41, 56]. Similar to other extrusion-printed Alg/Gel systems [59], the pristine hydrogel formulations (P1, P4) in this study showed limited post-deposition shape fidelity and relatively high swelling, reflecting the intrinsic softness and high water content of ionically crosslinked alginate–gelatine networks. The observed improvement in filament definition, pore preservation and dimensional stability upon addition of SiO_2 nanoparticles (P2, P3, P5, P6) is consistent with reports that inorganic nanofillers such as SiO_2 [60], cellulose nanocrystals [61], bioactive glass [62] or metal oxides [63] can act as rheological modifiers and mechanical reinforcements in Alg/Gel matrices, thereby enhancing print fidelity without compromising biocompatibility [35].

The predominantly amorphous character retained in both formulations, as shown by XRD is advantageous for drug delivery, as the amorphous SiO_2 surface presents a higher density of accessible silanol (Si–OH) groups that promote hydrogen-bonding interactions with polyphenols such as resveratrol, catechin, and gallic acid, contributing to the sustained-release behaviour of the composite scaffolds. Incorporation of mesoporous SiO_2 also had a pronounced effect on the swelling–degradation behaviour of the scaffolds. The reduction in equilibrium swelling ratio with increasing SiO_2 content and specific surface area mirrors observations in other Alg/Gel–SiO_2 [64] and Alg/Gel–inorganic nanocomposites [65], where surface silanol groups form hydrogen bonds and ionic interactions with alginate and gelatine, effectively restrict chain mobility. Comparable trends have been reported for alginate–gelatine hydrogels reinforced with Zn_2SiO_4 [66], TiO_2 or bioactive glass nanoparticles [67], where water uptake decreases and mechanical stability improves as the inorganic fraction increases. At the same time, all formulations in the present work retained a gradual, monotonic mass loss over 30 days, which is desirable for tissue engineering applications and aligns with the controlled degradation profiles described for optimized Alg/Gel scaffolds and other Alg-based printable inks [68].

The distinct behaviour of the SiO_2 2:1 versus SiO_2 4:1 formulations can be rationalized in light of literature on mesoporous SiO_2 design [69]. N_2 adsorption and XRD analyses in this study showed that SiO_2 2:1 possessed higher surface area [30], narrower pore size distribution and more pronounced mesoporosity than SiO_2 4:1, features known to increase drug loading capacity [24] and strengthen interfacial interactions with surrounding polymers [70]. Similar structure–property relationships have been reported for mesoporous SiO_2 systems where variations in surfactant/precursor [46] ratio or pore architecture modulate adsorption capacity and release kinetics of small molecules [8]. The lower swelling and slower degradation of P3 and P6 relative to their 4:1 counterpart at the same loading level therefore fit well with the concept that a higher density of accessible silanol sites on SiO_2 2:1 leads to a more tortuous diffusion pathway within the composite network.

With regard to the polyphenol delivery function, the UV–Vis release data obtained for the grape peel extract-loaded scaffolds are in line with the sustained, diffusion-controlled release [71] typically reported for polyphenols encapsulated in mesoporous SiO_2 carriers. Resveratrol and related phenolics such as catechin, ferulic acid and *p*-coumaric acid have been successfully loaded into MCM-41 [22], zeolitic and other mesoporous SiO_2 supports [45], where the confined pore environment protects the unstable *trans*-isomer and slows release relative to the free compound in solution. In those systems, early-stage release profiles likewise show a predominance of deep-UV absorbance from multiple phenolic species, while a distinct resveratrol band emerges more clearly only at longer times or higher loading, due to its lower molar proportion in complex mixtures and stronger retention within the mesopores. The modest resveratrol signal and progressive increase in 200–300 nm absorbance seen here over the first 3 h therefore support the interpretation that polyphenol transport is in an initial diffusion-controlled regime, with the crosslinked hydrogel/SiO_2 composite acting as a multi-scale barrier that moderates release.

When interpreted together, the LDH data and the SEM imaging suggest that the SiO_2-reinforced, grape peel extract-loaded scaffolds may modulate MC3T3-E1 cell adhesion and viability. Additionally, substrate rigidity has been shown to enhance the expression of focal adhesion proteins compared with less rigid substrates [72]. Meanwhile, the viscoelastic properties of the scaffolds slow cell spreading, providing a more gradual mechanical response to cell-generated forces [73].

Finally, the overall performance of the present SiO_2-reinforced Alg/Gel/XG scaffolds compares favourably with other inorganic-reinforced hydrogel systems proposed for bone and cartilage repair [74]. 3D-printed Alg/Gel constructs containing cellulose nanocrystals, mesoporous bioactive glass, or cerium-doped mesoporous SiO_2–CaO nanoparticles [75] have been shown to exhibit enhanced mechanical properties, controlled degradation, and improved osteogenic responses *in vitro* and *in vivo* [76] compared

with polymer-only controls. Likewise, alginate–gelatine hydrogels incorporating SiO_2 nanoparticles as injectable systems [77] have demonstrated good cytocompatibility and sustained release of bioactive agents, underscoring the versatility of SiO_2-reinforced Alg/Gel platforms for combined structural and therapeutic functions.

5. Conclusions

This study demonstrates that mesoporous SiO_2 nanoparticles synthesized by a CTAB-templated base-catalysed precipitation route with TEOS:CTAB molar ratios of 2:1 and 4:1 can be efficiently loaded with a polyphenol-rich *Vitis vinifera* L. peel extract and successfully incorporated into Alg/Gel/XG inks to produce 3D-printed composite scaffolds with tunable structural and biological properties. Among the two SiO_2 carriers, the 2:1 formulation exhibited the higher specific surface area and pore volume, greater peel extract uptake capacity, and more pronounced influence on scaffold swelling and degradation behaviour. Scaffolds containing SiO_2 2:1 at 2 wt% (P3) displayed the lowest equilibrium swelling ratio (106.96%) and among the most favourable degradation profiles over 30 days in PBS 1×. All composite inks displayed shear-thinning viscoelastic behaviour suitable for pneumatic extrusion, and printed scaffolds retained interconnected porosity compatible with cell infiltration. MC3T3-E1 preosteoblastic cells directly exposed to scaffold showed LDH release near baseline levels, indicating limited membrane damage under the tested conditions, with SEM revealing cell attachment within the macroporous network. These findings support the potential of grape peel extract-loaded SiO_2–Alg/Gel/XG scaffolds as multifunctional bioactive platforms combining agro-industrial waste valorisation, controlled polyphenol delivery, and a structural framework compatible with tissue engineering applications.

Future work should therefore focus on extending the release studies to longer time scales and under physiologically relevant conditions, including dynamic flow and enzymatic degradation, to more accurately capture *in vivo*–like release kinetics. A more detailed biological evaluation, incorporating osteogenic differentiation assays, angiogenic markers, and co-culture models with endothelial cells, would help clarify the regenerative potential of the bioactive composite scaffolds. Systematic variation of scaffold architecture and SiO_2 loading, could be used to optimize the balance between structural stability, diffusion pathways, and cell infiltration. Ultimately, *in vivo* studies in relevant bone or soft-tissue defect models will be essential to validate the capacity of grape peel extract-loaded SiO_2–hydrogel scaffolds to support tissue regeneration, neovascularization, and controlled local delivery of bioactives over clinically meaningful time frames.

By integrating a highly mesoporous, polyphenol-loaded SiO_2 phase into a 3D-printed Alg/Gel/XG framework with well-defined architecture and tunable swelling–degradation kinetics, the current work extends this concept toward antioxidant-enriched scaffolds that could be particularly attractive for oxidative-stress–laden environments such as bone defects or osteoarthritic cartilage.

List of Abbreviations

3D, three-dimensional; Alg/Gel/XG, alginate–gelatin–xanthan gum; SiO_2, silicon dioxide; CTAB, cetyltrimethylammonium bromide; TEOS, tetraethyl orthosilicate; XRD, X-ray diffraction; FTIR, Fourier-transform infrared spectroscopy; SEM/EDS, scanning electron microscopy/energy-dispersive X-ray spectroscopy; TG/DSC, thermogravimetry/differential scanning calorimetry; PBS, phosphate-buffered saline; LDH, lactate dehydrogenase; BET, Brunauer–Emmett–Teller; BJH, Barrett–Joyner–Halenda; ATR, attenuated total reflectance; LVR, linear viscoelastic region; CAD, computer-aided design; HMDS, hexamethyldisilazane; α-MEM, alpha minimum essential medium; DMSO, dimethyl sulfoxide; 2θ, diffraction angle (degrees); FWHM, full width at half maximum; Cu Kα, copper Kα X-ray radiation (λ = 0.15406 nm); a.u., arbitrary units; CPS, counts per second; °C, degrees Celsius.

Availability of Data and Materials

Data is contained within the article.

Author contributions

Conceptualization, A.T. and C.B.; methodology, A.T., A.-M.P., D.B., R.-C.P., D.-D.C. and C.-Ș.M.; investigation, A.T., A.-M.P., D.B., R.-C.P., D.-D.C. and C.-Ș.M.; formal analysis, A.T., D.B., R.-C.P., D.-D.C. and C.-Ș.M.; data curation, A.T.; writing – original draft preparation, A.T.; writing – review and editing, C.B. and E.L.; supervision, C.B. and E.L.; funding acquisition, E.L.; project administration, C.B. All authors have read and agreed to the published version of the manuscript.

Acknowledgements

The authors are grateful to the Romanian Government for providing access to the research infrastructure of the National Center for Micro and Nanomaterials through the National Program titled “Installations and Strategic Objectives of National Interest. We thank prof. dr. Ovidiu-Cristian Oprea for performing the thermal analysis measurements.

Financial support for the equipment was provided through grants awarded by the Ministry of Research, Innovation and Digitization, project number CNFIS-FDI-2026-F-1313.

Compliance with ethics guidelines

The authors declare no conflict of interest. This study does not contain any studies with human or animal subjects performed by any of the authors.

References

[1] N. Acero, J. Manrique, D. Muñoz-Mingarro, I. Martínez Solís, și F. Bosch, „Vitis vinifera L. Leaves as a Source of Phenolic Compounds with Anti-Inflammatory and Antioxidant Potential", *Antioxidants*, vol. 14, nr. 3, p. 279, mar. 2025, doi: 10.3390/antiox14030279.

[2] R. A. Bohara, N. Tabassum, M. P. Singh, G. Gigli, A. Ragusa, și S. Leporatti, „Recent Overview of Resveratrol's Beneficial Effects and Its Nano-Delivery Systems", *Molecules*, vol. 27, nr. 16, p. 5154, aug. 2022, doi: 10.3390/molecules27165154.

[3] A.-M. Brezoiu *et al.*, „Effect of Nanoconfinement of Polyphenolic Extract from Grape Pomace into Functionalized Mesoporous Silica on Its Biocompatibility and Radical Scavenging Activity", *Antioxidants*, vol. 9, nr. 8, p. 696, aug. 2020, doi: 10.3390/antiox9080696.

[4] B. S. Inbaraj, L.-H. Hua, și B.-H. Chen, „Comparative Study on Inhibition of Pancreatic Cancer Cells by Resveratrol Gold Nanoparticles and a Resveratrol Nanoemulsion Prepared from Grape Skin", *Pharmaceutics*, vol. 13, nr. 11, p. 1871, nov. 2021, doi: 10.3390/pharmaceutics13111871.

[5] R. Căpruciu și C. N. Gheorghiu, „Methods for Synthesis and Extraction of Resveratrol from Grapevine: Challenges and Advances in Compound Identification and Analysis", *Foods*, vol. 14, nr. 7, p. 1091, mar. 2025, doi: 10.3390/foods14071091.

[6] J. Bradić *et al.*, „From Vineyard to Hydrogel: Antioxidant, Anti-Inflammatory, and Regenerative Potential of Grape Skin Extract in Diabetic Wound Repair", *Pharmaceutics*, vol. 17, nr. 11, p. 1464, nov. 2025, doi: 10.3390/pharmaceutics17111464.

[7] E. Juère *et al.*, „*In Vitro* Dissolution, Cellular Membrane Permeability, and Anti-Inflammatory Response of Resveratrol-Encapsulated Mesoporous Silica Nanoparticles", *Mol. Pharmaceutics*, vol. 14, nr. 12, pp. 4431-4441, dec. 2017, doi: 10.1021/acs.molpharmaceut.7b00529.

[8] M. Sarfraz *et al.*, „Resveratrol-Laden Nano-Systems in the Cancer Environment: Views and Reviews", *Cancers*, vol. 15, nr. 18, p. 4499, sep. 2023, doi: 10.3390/cancers15184499.

[9] A. Smeriglio *et al.*, „Harnessing red grape pomace extract for sustainable broad-spectrum photoprotection in a reconstructed human epidermis model", *Front. Pharmacol.*, vol. 16, ian. 2026, doi: 10.3389/fphar.2025.1744377.

[10] X. Yang, J. Shi, Y. Chui, T. Wang, și Y. Xu, „Resveratrol-loaded nanofibrous scaffolds combined with menstrual blood stem cells for bone healing applications", *Tissue and Cell*, vol. 95, p. 102900, aug. 2025, doi: 10.1016/j.tice.2025.102900.

[11] X. Liu *et al.*, „Recent Advances in Resveratrol Derivatives: Structural Modifications and Biological Activities", *Molecules*, vol. 30, nr. 4, p. 958, feb. 2025, doi: 10.3390/molecules30040958.

[12] G. M. Alnafesah *et al.*, „Resveratrol functionalization of a collagen-based scaffold derived from amniotic membrane restores angiogenic activity and tissue regeneration in type 2 diabetic wound repair", *Tissue and Cell*, vol. 102, p. 103621, oct. 2026, doi: 10.1016/j.tice.2026.103621.

[13] H. Ma, Q. Zhou, J. Chang, și C. Wu, „Grape Seed-Inspired Smart Hydrogel Scaffolds for Melanoma Therapy and Wound Healing", *ACS Nano*, vol. 13, nr. 4, pp. 4302-4311, apr. 2019, doi: 10.1021/acsnano.8b09496.

[14] A. G. Luque-Alcaraz, J. A. Maldonado-Arriola, P. A. Hernández-Abril, M. E. Álvarez-Ramos, și C. N. Hernández-Téllez, „Zein Nanoparticles Loaded with Vitis vinifera L. Grape Pomace Extract: Synthesis and Characterization", *Nanomaterials*, vol. 15, nr. 7, p. 539, apr. 2025, doi: 10.3390/nano15070539.

[15] J. Liu, L. Yang, K. Liu, și F. Gao, „Hydrogel scaffolds in bone regeneration: Their promising roles in angiogenesis", *Front. Pharmacol.*, vol. 14, feb. 2023, doi: 10.3389/fphar.2023.1050954.

[16] „Phytochemical Compounds and Pharmacological Activities of Vitis vinifera L.: An Updated Review", *Biointerface Res Appl Chem*, vol. 11, nr. 6, pp. 13829-13849, mar. 2021, doi: 10.33263/BRIAC115.1382913849.

[17] A. Mollica *et al.*, „Phenolic Analysis and In Vitro Biological Activity of Red Wine, Pomace and Grape Seeds Oil Derived from Vitis vinifera L. cv. Montepulciano d'Abruzzo", *Antioxidants (Basel)*, vol. 10, nr. 11, p. 1704, oct. 2021, doi: 10.3390/antiox10111704.

[18] L. Peng *et al.*, „Polydopamine-functionalized 3D-printed scaffold co-loaded with resveratrol and NGF for enhanced neuronal differentiation under inflammatory stress", *Biomaterials Advances*, vol. 185, p. 214903, aug. 2026, doi: 10.1016/j.bioadv.2026.214903.

[19] J. Sharifi-Rad *et al.*, „Resveratrol-Based Nanoformulations as an Emerging Therapeutic Strategy for Cancer", *Front. Mol. Biosci.*, vol. 8, p. 649395, sep. 2021, doi: 10.3389/fmolb.2021.649395.

[20] L. Yarovaya, N. Waranuch, W. Wisuitiprot, și W. Khunkitti, „Effect of grape seed extract on skin fibroblasts exposed to UVA light and its photostability in sunscreen formulation", *J Cosmet Dermatol*, vol. 20, nr. 4, pp. 1271-1282, apr. 2021, doi: 10.1111/jocd.13711.

[21] D. del-Bosque, J. Vila-Crespo, V. Ruipérez, E. Fernández-Fernández, și J. M. Rodríguez-Nogales, „Silica-Calcium-Alginate Hydrogels for the Co-Immobilization of Glucose Oxidase and Catalase to Reduce the Glucose in Grape Must", *Gels*, vol. 9, nr. 4, p. 320, apr. 2023, doi: 10.3390/gels9040320.

[22] E. Juère *et al.*, „In Vitro Dissolution, Cellular Membrane Permeability, and Anti-Inflammatory Response of Resveratrol-Encapsulated Mesoporous Silica Nanoparticles", *Mol. Pharmaceutics*, vol. 14, nr. 12, pp. 4431-4441, dec. 2017, doi: 10.1021/acs.molpharmaceut.7b00529.

[23] Z. Chaudhary *et al.*, „Encapsulation and Controlled Release of Resveratrol Within Functionalized Mesoporous Silica Nanoparticles for Prostate Cancer Therapy", *Front. Bioeng. Biotechnol.*, vol. 7, p. 225, sep. 2019, doi: 10.3389/fbioe.2019.00225.

[24] E. V. Parfenyuk, E. S. Dolinina, și A. S. Kraev, „Synthesis and study of organo-modified silica based hydrogels: Rheological properties and drug release kinetics", *J Biomed Mater Res*, vol. 112, nr. 6, p. e35418, iun. 2024, doi: 10.1002/jbm.b.35418.

[25] L. Qin, Y. He, X. Zhao, T. Zhang, Y. Qin, și A. Du, „Preparation, Characterization, and In Vitro Sustained Release Profile of Resveratrol-Loaded Silica Aerogel", *Molecules*, vol. 25, nr. 12, p. 2752, iun. 2020, doi: 10.3390/molecules25122752.

[26] Z. Nan, M. Wang, și B. Yan, „In Situ Investigation on the Formation Mechanism of MCM-41 Mesoporous Silica by Microcalorimetry", *J. Chem. Eng. Data*, vol. 54, nr. 1, pp. 83-89, ian. 2009, doi: 10.1021/je8006502.

[27] S. Ameli, M. Nourani, N. Bakhshi, B. Salemi, E. Assadpour, și S. M. Jafari, „Alginate-gelatin composite hydrogels for

encapsulating Aloe vera extract; optimization, characterization, and release kinetics", *Carbohydrate Polymer Technologies and Applications*, vol. 9, p. 100717, mar. 2025, doi: 10.1016/j.carpta.2025.100717.

[28] G. Do Espirito Santo *et al.*, „3D-Printed Composite Scaffolds Containing SiO_2 for Bone Regeneration in *In Vivo* Models: A Systematic Review", *ACS Omega*, vol. 11, nr. 20, pp. 29268-29279, mai 2026, doi: 10.1021/acsomega.5c10447.

[29] F. Perin *et al.*, „Modeling a Dynamic Printability Window on Polysaccharide Blend Inks for Extrusion Bioprinting", *ACS Biomater. Sci. Eng.*, vol. 9, nr. 3, pp. 1320-1331, mar. 2023, doi: 10.1021/acsbiomaterials.2c01143.

[30] M. Monavari *et al.*, „3D printing of alginate dialdehyde-gelatin (ADA-GEL) hydrogels incorporating phytotherapeutic icariin loaded mesoporous SiO2-CaO nanoparticles for bone tissue engineering", *Materials Science and Engineering: C*, vol. 131, p. 112470, dec. 2021, doi: 10.1016/j.msec.2021.112470.

[31] J. Sun, C. Chen, B. Zhang, C. Yao, și Y. Zhang, „Advances in 3D-printed scaffold technologies for bone defect repair: materials, biomechanics, and clinical prospects", *BioMedical Engineering OnLine*, vol. 24, nr. 1, p. 51, apr. 2025, doi: 10.1186/s12938-025-01381-w.

[32] M. M. Marin *et al.*, „Microbial Polysaccharide-Based Formulation with Silica Nanoparticles; A New Hydrogel Nanocomposite for 3D Printing", *Gels*, vol. 9, nr. 5, p. 425, mai 2023, doi: 10.3390/gels9050425.

[33] D.-D. Cristea, E. Liciu, A. Trifan, și C. Bălan, „Volumetric Control vs. Pneumatic Pressure: A Comparative Analysis of Extrusion in 3D Bioprinting", *Micromachines*, vol. 17, nr. 5, p. 521, mai 2026, doi: 10.3390/mi17050521.

[34] D. Oh, M. Shirzad, M. C. Kim, E.-J. Chung, și S. Y. Nam, „Rheology-informed hierarchical machine learning model for the prediction of printing resolution in extrusion-based bioprinting", *International Journal of Bioprinting*, vol. 9, nr. 6, p. 1280, aug. 2023, doi: 10.36922/ijb.1280.

[35] E. Luzzi, M. de Salzano de Luna, D. Caputo, G. Filippone, și P. Aprea, „Printability Metrics in Direct Ink Writing: Critical Review of the Literature and Novel Perspective Based on Dimensional Analysis", *Advanced Materials Technologies*, vol. 10, nr. 22, p. e01282, 2025, doi: 10.1002/admt.202501282.

[36] Y. Bao, „Recent Trends in Advanced Photoinitiators for Vat Photopolymerization 3D Printing", *Macromol. Rapid Commun.*, vol. 43, nr. 14, p. 2200202, iul. 2022, doi: 10.1002/marc.202200202.

[37] R. V. Barrulas și M. C. Corvo, „Rheology in Product Development: An Insight into 3D Printing of Hydrogels and Aerogels", *Gels*, vol. 9, nr. 12, p. 986, dec. 2023, doi: 10.3390/gels9120986.

[38] D. Coblas, D. Broboana, și C. Balan, „Correlation between large amplitude oscillatory shear (LAOS) and steady shear of soft solids at the onset of the fluid rheological behavior", *Polymer*, vol. 104, pp. 215-226, nov. 2016, doi: 10.1016/j.polymer.2016.06.003.

[39] „Illustrae - Professional Scientific Illustration Platform". Data accesării: 18 februarie 2026. [Online]. Disponibil la: https://illustrae.co/dashboard

[40] A. Trifan *et al.*, „Effect of Phosphate Phase Incorporation on 3D-Printed Hydrogel Scaffolds: Towards Customizable Bone Graft Materials", *Gels*, vol. 11, nr. 8, p. 665, aug. 2025, doi: 10.3390/gels11080665.

[41] „MC3T3-E1 Subclone 4 - CRL-2593 | ATCC", https://www.atcc.org. Data accesării: 26 februarie 2026. [Online]. Disponibil la: https://www.atcc.org/products/crl-2593

[42] „OriginLab - Origin and OriginPro - Data Analysis and Graphing Software". Data accesării: 29 iunie 2026. [Online]. Disponibil la: https://www.originlab.com/

[43] F. Putz *et al.*, „The influence of drying and calcination on surface chemistry, pore structure and mechanical properties of hierarchically organized porous silica monoliths", *Microporous and Mesoporous Materials*, vol. 288, p. 109578, nov. 2019, doi: 10.1016/j.micromeso.2019.109578.

[44] Y. Han, L. Zhang, și W. Yang, „Synthesis of Mesoporous Silica Using the Sol–Gel Approach: Adjusting Architecture and Composition for Novel Applications", *Nanomaterials (Basel)*, vol. 14, nr. 11, p. 903, mai 2024, doi: 10.3390/nano14110903.

[45] N. I. Vazquez, Z. Gonzalez, B. Ferrari, și Y. Castro, „Synthesis of mesoporous silica nanoparticles by sol–gel as nanocontainer for future drug delivery applications", *Bol Soc Esp Ceram Vidr*, vol. 56, nr. 3, pp. 139-145, mai 2017, doi: 10.1016/j.bsecv.2017.03.002.

[46] R. R. Castillo, L. de la Torre, F. García-Ochoa, M. Ladero, și M. Vallet-Regí, „Production of MCM-41 Nanoparticles with Control of Particle Size and Structural Properties: Optimizing Operational Conditions during Scale-Up", *Int J Mol Sci*, vol. 21, nr. 21, p. 7899, oct. 2020, doi: 10.3390/ijms21217899.

[47] V. Candela-Noguera, M. Alfonso, P. Amorós, E. Aznar, M. D. Marcos, și R. Martínez-Máñez, „In-depth study of factors affecting the formation of MCM-41-type mesoporous silica nanoparticles", *Microporous and Mesoporous Materials*, vol. 363, p. 112840, ian. 2024, doi: 10.1016/j.micromeso.2023.112840.

[48] J. L. Aleixandre-Tudo, H. Nieuwoudt, A. Olivieri, J. L. Aleixandre, și W. du Toit, „Phenolic profiling of grapes, fermenting samples and wines using UV-Visible spectroscopy with chemometrics", *Food Control*, vol. 85, pp. 11-22, mar. 2018, doi: 10.1016/j.foodcont.2017.09.014.

[49] Y. Song *et al.*, „Grape skin extract prevents UV irradiation induced DNA damage of normal human epidermal keratinocytes cells", *Journal of Berry Research*, vol. 10, nr. 4, pp. 585-601, dec. 2020, doi: 10.3233/JBR-190519.

[50] M. Verma, A. Nisha, M. Bathla, și A. Acharya, „Resveratrol-Encapsulated Glutathione-Modified Robust Mesoporous Silica Nanoparticles as an Antibacterial and Antibiofilm Coating Agent for Medical Devices", *ACS Appl. Mater. Interfaces*, vol. 15, nr. 50, pp. 58212-58229, dec. 2023, doi: 10.1021/acsami.3c13733.

[51] O.-R. Bancuta *et al.*, „FT-IR AND UV-VIS CHARACTERIZATION OF GRAPE EXTRACTS USED AS ANTIOXIDANTS IN POLYMERS".

[52] R. Lakra, M. S. Kiran, și K. P. Sai, „Fabrication of homobifunctional crosslinker stabilized collagen for biomedical application", *Biomed Mater*, vol. 10, nr. 6, p. 065015, nov. 2015, doi: 10.1088/1748-6041/10/6/065015.

[53] J. Si *et al.*, „Osteogenic differentiation capabilities of multiarm PEG hydrogels: involvement of gel–gel-phase separation in cell differentiation", *Polym J*, vol. 57, nr. 4, pp. 407-417, apr. 2025, doi: 10.1038/s41428-024-00955-0.

[54] S. L. Haag, N. R. Schiele, și M. T. Bernards, „Enhancement and mechanisms of MC3T3-E1 osteoblast-like cell adhesion to albumin through calcium exposure", *Biotechnol Appl Biochem*, vol. 69, nr. 2, pp. 492-502, apr. 2022, doi: 10.1002/bab.2126.

[55] M. Carles-Carner, L. S. Saleh, și S. J. Bryant, „The effects of hydroxyapatite nanoparticles embedded in a MMP-sensitive photoclickable PEG hydrogel on encapsulated MC3T3-E1 pre-osteoblasts", *Biomed. Mater.*, vol. 13, nr. 4, p. 045009, mai 2018, doi: 10.1088/1748-605X/aabb31.

[56] C. Wu, M. Chen, T. Zheng, și X. Yang, „Effect of surface roughness on the initial response of MC3T3-E1 cells cultured on polished titanium alloy", *Biomed Mater Eng*, vol. 26 Suppl 1, pp. S155-164, 2015, doi: 10.3233/BME-151301.

[57] A. Mahran *et al.*, „Functional enzyme delivery via surface-modified mesoporous silica nanoparticles in 3D printed nanocomposite hydrogels", *European Journal of*

Pharmaceutical Sciences, vol. 211, p. 107132, aug. 2025, doi: 10.1016/j.ejps.2025.107132.

[58] A. Trifan *et al.*, „Developing Bioengineered 3D-Printed Composite Scaffolds with Antimicrobial Potential for Bone Tissue Regeneration", *J Funct Biomater*, vol. 16, nr. 6, p. 227, iun. 2025, doi: 10.3390/jfb16060227.

[59] J. V. Bradic *et al.*, „Formulation of Alginate–Gelatin Hydrogels within a Circular Economy Framework: Controlled Release of Grape Skin Extract via Gelatin Content Modulation", în *Book of Proceedings*, Kragujevac: University, Institute for Information Technologies, 2025. doi: 10.46793/ICCBIKG25.685B.

[60] M. M. Mahamoud, Y. Kuwahara, H. Ihara, și M. Takafuji, „Impact of Silica Nanoparticles on Mechanical Properties and Self-Healing Performance of PVA Hydrogels", *Polymers*, vol. 17, nr. 21, p. 2883, oct. 2025, doi: 10.3390/polym17212883.

[61] A. Mahran *et al.*, „Functional enzyme delivery via surface-modified mesoporous silica nanoparticles in 3D printed nanocomposite hydrogels", *European Journal of Pharmaceutical Sciences*, vol. 211, p. 107132, aug. 2025, doi: 10.1016/j.ejps.2025.107132.

[62] X. Chen, T. Wu, Y. Bu, H. Yan, și Q. Lin, „Fabrication and Biomedical Application of Alginate Composite Hydrogels in Bone Tissue Engineering: A Review", *Int J Mol Sci*, vol. 25, nr. 14, p. 7810, iul. 2024, doi: 10.3390/ijms25147810.

[63] E. Wu *et al.*, „Application of gelatin-based composites in bone tissue engineering", *Heliyon*, vol. 10, nr. 16, p. e36258, aug. 2024, doi: 10.1016/j.heliyon.2024.e36258.

[64] C. Kaliampakou, N. Lagopati, E. Pavlatou, și C. A. Charitidis, „Alginate–Gelatin Hydrogel Scaffolds; An Optimization of Post-Printing Treatment for Enhanced Degradation and Swelling Behavior", *Gels*, vol. 9, p. 857, oct. 2023, doi: 10.3390/gels9110857.

[65] U. Shahid *et al.*, „Development of a Ce-doped hydroxyapatite–sodium alginate biocomposite for bone and dental implants", *New J. Chem.*, vol. 47, nr. 15, pp. 7217-7224, apr. 2023, doi: 10.1039/D2NJ06203H.

[66] Y. Han *et al.*, „Study of bioactive 3D-printed scaffolds incorporating zinc-based MOF for bone defect repair and anti-inflammatory applications", *Mater Today Bio*, vol. 32, p. 101884, mai 2025, doi: 10.1016/j.mtbio.2025.101884.

[67] E. Shukrun, I. Cooperstein, și S. Magdassi, „3D-Printed Organic–Ceramic Complex Hybrid Structures with High Silica Content", *Advanced Science*, vol. 5, nr. 8, p. 1800061, aug. 2018, doi: 10.1002/advs.201800061.

[68] J. Cao, B. Wu, P. Yuan, Y. Liu, și C. Hu, „Research Progress of Sodium Alginate-Based Hydrogels in Biomedical Engineering", *Gels*, vol. 11, nr. 9, p. 758, sep. 2025, doi: 10.3390/gels11090758.

[69] I. Trendafilova și M. Popova, „Porous Silica Nanomaterials as Carriers of Biologically Active Natural Polyphenols: Effect of Structure and Surface Modification", *Pharmaceutics*, vol. 16, nr. 8, p. 1004, iul. 2024, doi: 10.3390/pharmaceutics16081004.

[70] M. Lin *et al.*, „Resveratrol-modified mesoporous silica nanoparticle for tumor-targeted therapy of gastric cancer", *Bioengineered*, vol. 12, nr. 1, pp. 6343-6353, ian. 2021, doi: 10.1080/21655979.2021.1971507.

[71] D. Marinheiro, B. Ferreira, P. Oskoei, H. Oliveira, și A. Daniel-da-Silva, „Encapsulation and Enhanced Release of Resveratrol from Mesoporous Silica Nanoparticles for Melanoma Therapy", *Materials*, vol. 14, nr. 6, p. 1382, mar. 2021, doi: 10.3390/ma14061382.

[72] Y. Zhang *et al.*, „Osteogenesis-Related Behavior of MC3T3-E1 Cells on Substrates with Tunable Stiffness", *BioMed Research International*, vol. 2018, nr. 1, p. 4025083, 2018, doi: 10.1155/2018/4025083.

[73] J. Zuo și S. Ma, „Resveratrol-laden mesoporous silica nanoparticles regulate the autophagy and apoptosis via ROS-mediated p38-MAPK/HIF-1a /p53 signaling in hypertrophic scar fibroblasts", *Heliyon*, vol. 10, nr. 4, p. e24985, feb. 2024, doi: 10.1016/j.heliyon.2024.e24985.

[74] B. Wei *et al.*, „Gelatin methacrylate hydrogel scaffold carrying resveratrol-loaded solid lipid nanoparticles for enhancement of osteogenic differentiation of BMSCs and effective bone regeneration", *Regenerative Biomaterials*, vol. 8, nr. 5, p. rbab044, aug. 2021, doi: 10.1093/rb/rbab044.

[75] X.-L. Liu *et al.*, „Nacre-mimetic cerium-doped nano-hydroxyapatite/chitosan layered composite scaffolds regulate bone regeneration via OPG/RANKL signaling pathway", *J Nanobiotechnol*, vol. 21, nr. 1, p. 259, aug. 2023, doi: 10.1186/s12951-023-01988-y.

[76] J. S. Vuković *et al.*, „In Vitro and In Vivo Biocompatible and Controlled Resveratrol Release Performances of HEMA/Alginate and HEMA/Gelatin IPN Hydrogel Scaffolds", *Polymers*, vol. 14, nr. 20, p. 4459, oct. 2022, doi: 10.3390/polym14204459.

[77] G. Codispoti *et al.*, „Visible light-mediated crosslinked methacrylated gellan gum nanocomposite hydrogel: Physicochemical characterization and *in vivo* safety", *Materials & Design*, p. 116244, mai 2026, doi: 10.1016/j.matdes.2026.116244.

Supplementary Files

This is a list of supplementary files associated with this preprint. Click to download.

- manuscripthighlights.docx
- Graphicalabstract.png